Dimensional Dependence of Light Interaction with Nanowires

A Thesis

Submitted to the Faculty

of

Drexel University

by

Zhihuan Wang

in partial fulfillment of the

requirements for the degree

of

Doctor of Philosophy

September 2016

DEDICATIONS

This thesis is dedicated to my family. Their unconditional support and love was the foundation of success for my graduate study. I want you to know that I love you so much and this thesis was only possible thanks to you.

ACKNOWLEDGMENTS

This work would not have been possible without the support of my advisor, Dr. Bahram Nabet. His guidance helped to shape and provided much needed focus to my work. I would like to thank my dissertation committee of Dr. Timothy Kurzweg, Dr. Baris Taskin, Dr. Nagarajan Kandasamy, and Dr. Goran Karapetrov for their support and insight throughout my research.

I would also like to thank my friends in the Photonics Lab for all the help and support they provided, and especially for providing such a friendly and awesome place to work and study at. Weston Aenchbacher and Shrenik Vora have spent countless hours listening to me talk about my research, helping me flesh out my ideas. And a special thanks to Jiajia Liu for proofreading all of my work and for encouraging me throughout my graduate work.

TABLE OF CONTENTS

LIST OF TABLES

LIST OF FIGURES

ABSTRACT

Dimensional Dependence of Light Interaction with Nanowires
Zhihuan Wang
Advisor: Dr. Bahram Nabet

Semiconductor nanowires have been used in a variety of passive and active optoelectronic devices including waveguides, photodetectors, solar cells, LEDs, Lasers, sensors, and optical antennas. We review the optical properties of these nanowires in terms of absorption, guiding, and radiation of light, which may be termed light management. Analysis of the interaction of light with long cylindrical structures with sub-wavelength diameters identifies radial resonant modes, such as Leaky Mode Resonances, or Whispering Gallery modes. The two-dimensional treatment should incorporate axial variations in volumetric modes which have so far been presented in terms of Fabry-Perot, and Helical resonance modes. We report on FDTD simulations with the aim of identifying the dependence of these modes on: geometry (length, width), tapering, shape (cylindrical, hexagonal), core-shell versus core-only, and dielectric cores with semiconductor shells. This demonstrates how NWs form excellent optical cavities without the need for top and bottom mirrors. However, optically equivalent structures such as hexagonal and cylindrical wires can have very different optoelectronic properties meaning that light management alone does not sufficiently describe the observed enhancement in upward (absorption) and downward transitions (emission) of light in nanowires; rather, the electronic transition rates should be considered. We discuss this rate-management scheme showing its strong dimensional dependence, making a case for photonic integrated circuits that can take advantage of the confluence of the desirable optical and electronic properties of these nanostructures.

CHAPTER 1

INTRODUCTION

The development of sophisticated growth techniques for layered semiconductor structures has stimulated a large body of new work in semiconductor physics over the last fifteen years or so. Undoubtedly, much of this interest was further stimulated by the possibility of novel physics and applications in electronic transport. New physical discovered in inversion channels and heterostructures, and the first heterostructure electronic devices, such as modulation-doped field-effect transistors and heterojuntion bipolar transistors, are now being commercially exploited. Linear optical spectroscopic techniques, such as absorption, luminescnence and modulation spectroscopy, have for a long time been important tools in understanding the basic physics of semiconductor materials. Also over the last fifteen years or so, semiconductor optical and optioelectronic properties have become of increasing technological importance in their own right. The ever-growing application of semiconductor diode lasers and related optoelectronic technology in communications and consumer products has helped to give yet further impetus to research on semiconductor optical properties.

The successes of semiconductor optoelectronics and promising physical mechanisms and novel devices using quantum-confined structures have, furthermore, enlivened the debate over possible applications of optics for other functions such as logic and switching in communications and computation.

It is important to emphasize at the outset that quantum confinement and produce not only quantitative but also qualitative differences in physics from that in bulk structures, which is of course another major motivation for the interest in them. There are many examples of these differences. The optical absorption spectrum breaks up into a series of steps associated with the quantum-

confined electron and hole levels. Excitonic effects become much stronger because of the quantum confinement, giving clear absorption resonances even at room temperature. The relative importance of direct Coulomb screening and exchange effects is quite different in quantum wells (the Coulomb screening is relatively much weaker), giving very different optical saturation behaviour.

1.1 Background

1.2 Problem Statement

1.3 Literature Review

1.4 Outline of Chapters

This thesis is structured as follows. The data used for this analysis are presented in Chapter 2. After introducing the corrections and data analysis methods, Chapter **??** presents our findings for individual and mean bolometric corrections. Chapter **??** presents our methods and findings for estimating dust reddening associated with a subset of our quasars. The statistical methods used in this chapter are outlined in more detail in Appendix **??**. In Chapter **??**, we apply the corrections from Chapter **??** to our SEDs and use estimated black hole masses to study changes in the SEDs with the properties of the central black hole. Finally, we present our conclusions in Chapter 7. Throughout this work we use a ΛCDM cosmology with $H_0 = 71$ km s^{-1} Mpc^{-1}, $\Omega_\Lambda = 0.734$, and $\Omega_m = 0.266$, consistent with the *Wilkinson Microwave Anisotropy Probe* 7 cosmology[?] .

CHAPTER 2

OPTICAL ENHANCEMENT OF CORE-SHELL NANOWIRE

Given that the profound enhancement of optoeletronic properties of nanowires is the major theme of this dissertation, it is dutiful to first summarize the major experimental charateristics of Core-Shell nanowires (CSNWs)

Electron systems in lower dimensions are adequately treated through perturbation methods. For 1D electron systems (1DES) the correlations among electrons are much more significant due to higher degrees of confinement. The electron can either be moving to the left or right and any small or localized interaction can cause a collective response from the whole system. This is the condition of broken symmetry, in which the overall status of the system has to be reformulated. For a 2DES, a broken symmetry occurs at very low densityies of fermions, in which formation of a Wigner lattice is expected, which is due to the Coulombic interactions of electrons. Intererstingly for a 1DES, the direction of movement for fermions is restricted to the left or right. Consequently, the density of the sytem becomes irrelevant with respect to the determination of the status of the system. Such a 1D many electron system is often called a *Lüfinger* Liquid, as he was the first person who successfully formulated these systems.

Importantly, a 1DES can experimentally be realized in various material systems. These include carbon nanotubes, electrons at the edges of a 2DES, and in nanowires.

A core-shell nanowire (CSNW) is a quasi-one dimensional structure with a wide band gap materials, such as AlGaAs, wrapping around a low band gap semiconductor, such as GaAs.

It is expected that the lower dimensionality in CSNW to have a significant influence on both optical and electrical properties of the structure. Fot instantce,

Electrically it is important account for the electron correlations in order to determine the behavior of the structure. The significant values ofr exchange and correlation energies in 1DES. makes them an interesting candidate for probing ther energy dynamics. This, however, imposes various experimental challenges and theoretical considerations and are deferred to future investigations.

2.1 Growth of Nanowires

Freestanding quasi-one-dimensional semiconductor nanostructures (nanowires) based on III-V compound semiconductors, owing to their unique physical properties, are considered ideal building blocks for the realization of photonic and electronic nanodevices.

Currently, two bottom-up approaches to the fabrication of freestanding nanowires are considered: (i) selective area epitaxy (SAE)[2] and (ii) metal-catalyst assisted grouth through the so-called vapor-liquid-solid (VLS) mechanism[1,3]. The latter method relies on the alloying of a metal catalyst (usually Au) nanoparticle with the semiconductor constituent elements, supplied through a vapor phse. The as-formed alloy acts as an initial nucleation site for the material and further guides the nanowire growth, the diameter of the nanowire being controlled by that of the metal nanoparticle.

An advantage of the VLS method over SAE is that it does not require nanolithograpic processing of the substrate; furthermore, it is compatible with most advanced epitaxial grouth techniques for III-V compounds, such as molecular beam epitaxy, chemical beam epitaxy, and metalorganic vapor phase epitaxy (MOVPE).

GaAs nanowires were grwon by low (50mbar) pressure MOVPE using an Aixtron reactor model AIX200 RD. TMGa and TBAs were used as gallium and arsenic precursors, respectively. Au nanoparticle deposited on $(\bar{1}\bar{1}\bar{1})B$ GaAs were used to catalyze the nanowire growth. To this purpose, VGF-grown semi-insulating (undoped) GaAs wafers oriented $(\bar{1}\bar{1}\bar{1})B$ were used. The substrates were then first degreased in isopropanol vapors, etched in $4H_2SO_4 : 1H_2O_2 : 2H_2O$ solution for 8 min at

around 40 °c, ringsed in de-ionized water and finally dried under pure N_2. Au nanoparticles with $\tilde{6}0$ nm diameters were prepared by reaction of $HAuCl_4$ with sodium citrate in aqueous solution and randomly deposited on the as-prepared GaAs surface by dropping a small amount of colloidal solution onto the substrate. The solvent (water) was then evaporated by holding the samples on a hot plate (in air) or a few minutes; Au nanoparticle surface densities thus achieved ranged around (1-4).

After loading the sample into the reactor chamber, its temperature was raised, and sample annealing was then performed for 10 min to absorb GaAs surface oxides and organic residules originating from the Au nanoparticle synthesis. This annealing step would also allow the initial uptake of Ga atoms from the GaAs substrate into the Au nanoparticles.

2.2 Scanning Electron Microscopy Images

Figure 1a is top view SEM image of nanowires of 100nm diameter core of GaAs, and 40nm thick AlGaAs, with the inset showing a magnified image that demonstrates the rather sparse distribution of the wires. Figure 1b shows the reflectivity of a GaAs wafer on which 50nm thin film of AlGaAs is grown, and compares this to the reflectivity spectrum of a Si substrate. As expected, about 30% to 55% of a normally incident light is reflected in bulk Si and GaAs, with a sharp change for wavelengths near their respective band gaps. Figure 1c contrasts this with the measured absorption spectrum of two types of GaAs core, AlGaAs shell (CS) nanowires (BW): those grown on a GaAs substrate (black), and the others heteroepitaxially grown on a Si substrate (red). The spectra show that both cases have the signature change of reflectivity at bandgap of GaAs, i.e., these are due to the GaAs/AlGaAs CSNWs, not the substrate. Importantly, for the wavelength range of 700-1200nm these core-shells which only occupy 15of the volume compared to thin films of the same height, reflect 2-4% of light for the CSNWs grown on Si, and 3-7% of light for those grown on GaAs substrate. The beam-width of the incident light being 1m, this shows that only a few NWs are interrogated by light and, normalized to volume, these wires absorb more than two orders of magnitude more light than their thin-film counterparts.

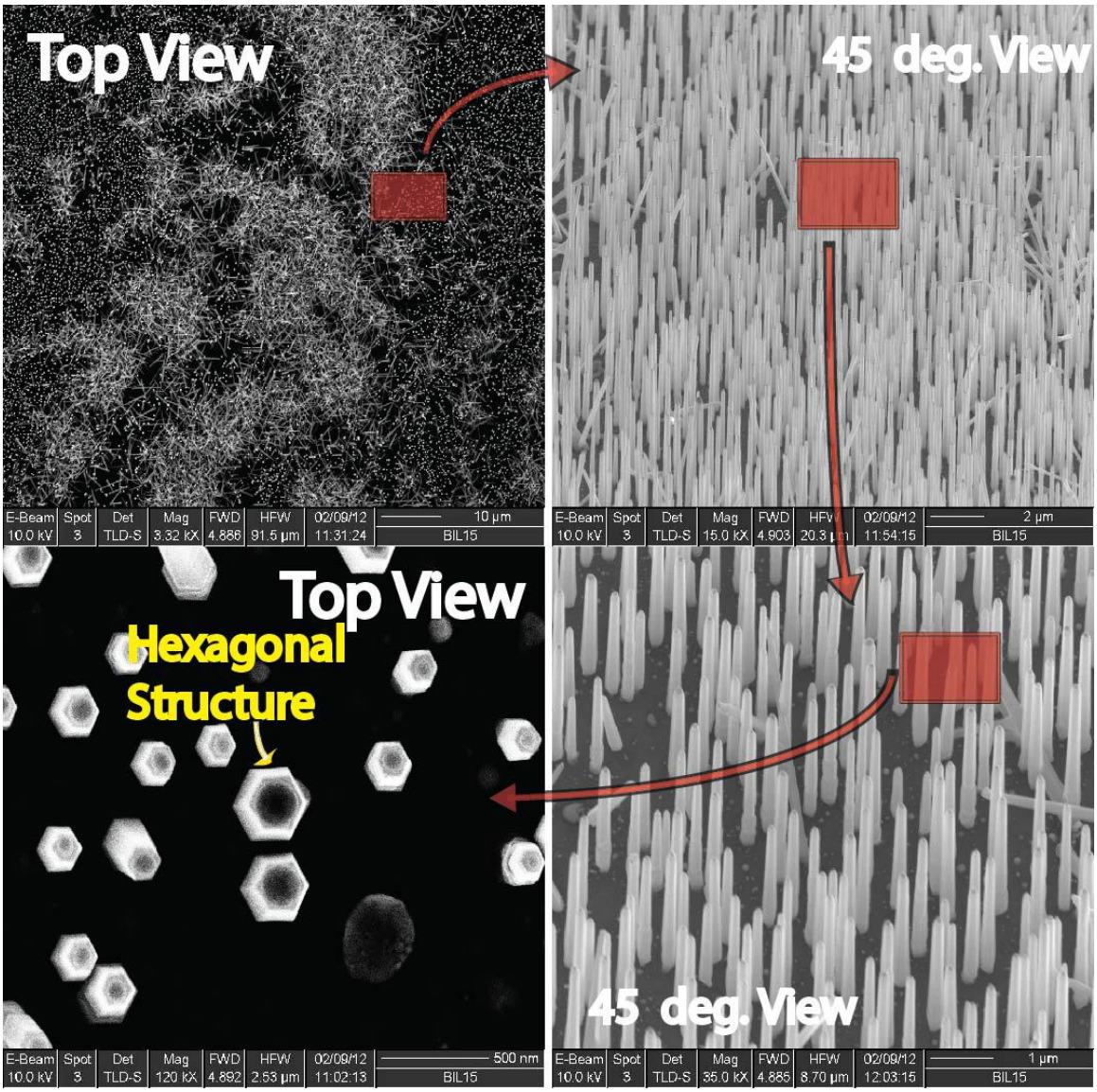

Figure 2.1 Scanning Electron Microscopy image of as-grown GaAs/AlGaAs core-shell nanowires on Sitaken at different magnifications and view angles

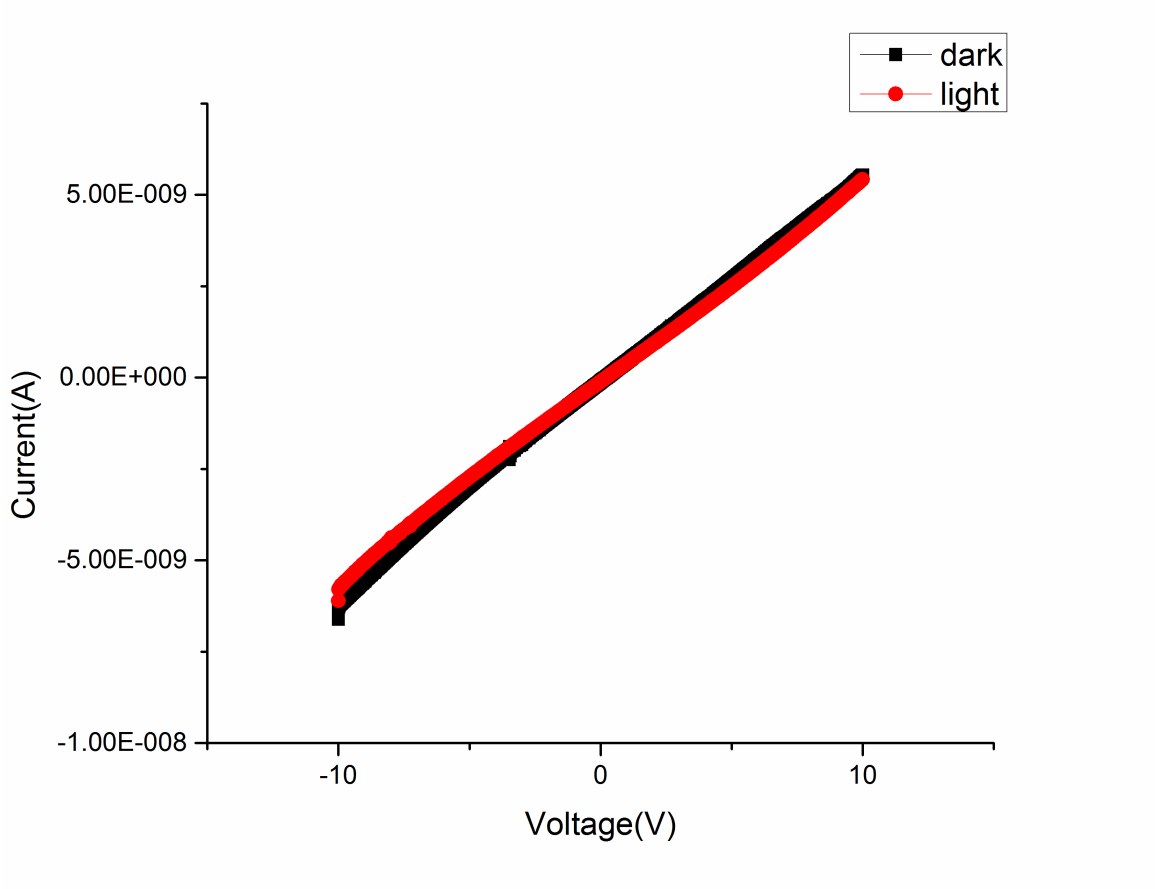

Figure 2.2 Current versus Voltage Measurment under illumination of Core-Shell Nanowire Grown on Si

2.3 Electrical Characterization of Nanowire

2.4 Absorption Enhancement

2.5 Emission Enhancement

2.6 Lasing

Photoluminescence (PL) of bulk GaAs to nanowires grown on GaAs, and on two directions of Si showed that normalized to the fraction of the volume that these wires occupy, nealy 10,000 times more brightness is observed in these wires compared to hin-film. In the case of stimulated emission of light, the photon mode density $(1 + u_\varepsilon)$ plays a crucial role. Figure is the photoluminescence

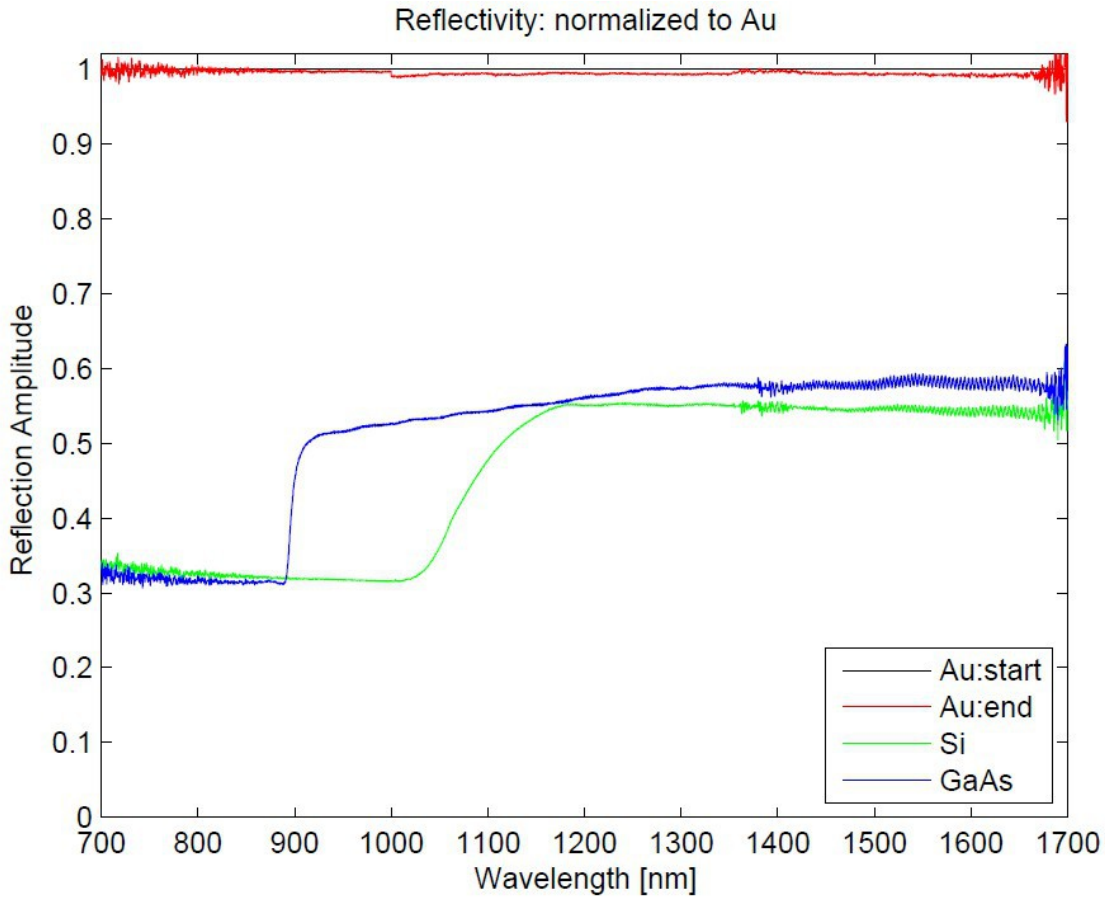

Figure 2.3 Reflective Measurement for Bulk GaAs and Si

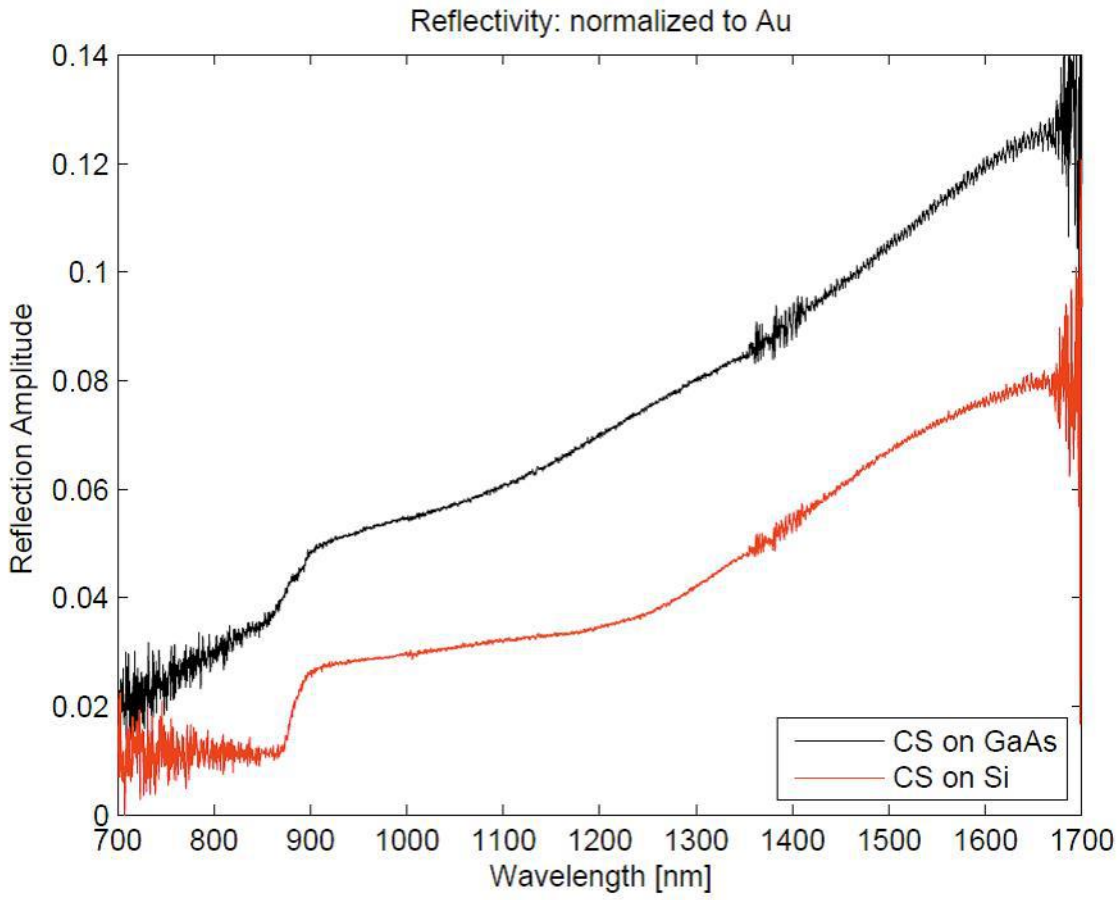

Figure 2.4 Reflective Measurement for Core-Shell Nanowires Grown on Bulk GaAs and Si

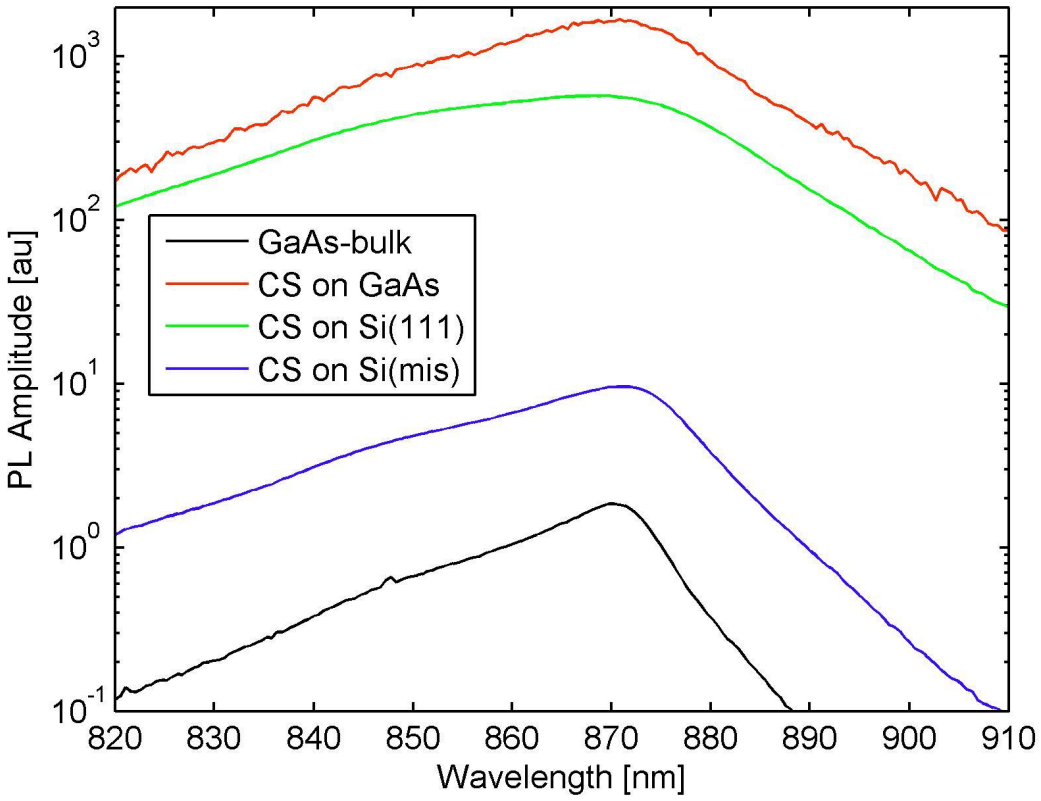

Figure 2.5 Photoluminescence Experiment for Core-Shell Nanowires Grown on Bulk GaAs and Si

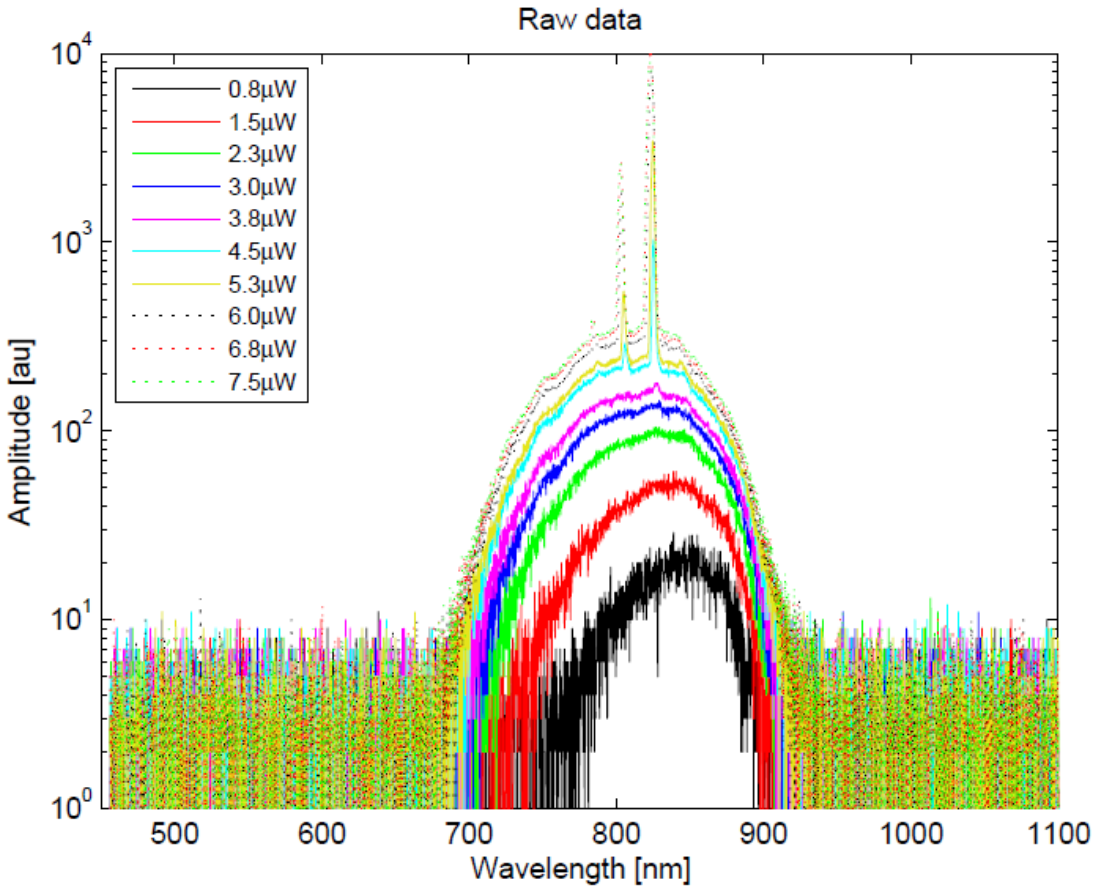

Figure 2.6 Micro-Photoluminescence measurements with fs-pulsed, 532-nm laser excitation at 250kHz repetition rate shows lasing of the as-grown wires.

(PL) spectrum at various optical pump intensities. As the excitation laser power increase beyond $\tilde{5}$ a sudden and highly nonlinear increase in the emission intensity is observed, with pronounced peaks emerging from 800nm to 850nm that rapidly grows to become several orders of magnitude stronger than the background emission. The laser amplitude vs. excitation power demonstrates a threshold of around $\tilde{5}$, followed by saturation near $\tilde{1}2$. The sharp peak has a full width half maximum (FWHM) that varies from 1.5 to 3.5 nm. This remarkable behavior is achieved in the as-grown wires with no vertical structure.

CHAPTER 3

LIGHT CONFINEMENT IN SUB-WAVELENGTH NANO-STRUCTURE

3.1 Light and Nanowire

3.1.1 Leaky Mode Resonance

Interaction of light with a dielectric or metallic cylindrical medium is analyzed by solving Maxwell's equations with the appropriate boundary conditions in the classical waveguide theory [80] which leads to highly confined modes in optical fibers and microscale dielectric resonators. In an infinitely long cylinder, even at deep sub-wavelength diameters this results in a characteristic equation the solution to which are the transverse magnetic (TM) and transverse electric (TE) resonant modes. We can define the electromagnetic modes of localized resonators as time-harmonic solutions of the form to the source-free Maxwell equations. This solution shows that the longitudinal field component distributes outside the NW, and is in resonance with the natural modes, such as TE11, TM02, etc., supported by the NW. These modes have been termed leaky-mode resonances (LMR) [81, 82], and provide an intuitive tool to facilitate the understanding and optimization of the resonance effect in such nano-structures. We replicate these results using MEEP, a widely used open-source finite-difference time-domain (FDTD) simulation package [83], to identify how light is confined in an infinitely long GaAs nanowire. The top row of Fig. 1 shows several configurations of TM LMR modes for a NW with diameter of 220nm, with excitation single wavelength light being incident parallel to the NW axis. The blue and red color codes represent the polarization of the electric fields. The TE modes are primarily identical to the TM modes shown here with the electric and magnetic fields

exchanged. If the light is incident with an arbitrary angle, then so-called hybrid HE and EH leaky modes will be excited instead of the pure TE or TM mode. The bottom row of Fig. 1 shows the directional energy flux density of the electromagnetic field, the Poynting vector, at different time frames with light being incident perpendicular to the NW axis from the right side. The light is seen to propagate from the right and then mostly remain confined at the left part of the cylinder. It is notable that in either case the light energy is spatially distributed along the cross section of the wire but, as expected from a 2D treatment does not vary axially. Figure 1 demonstrates that the LMR can gently confine light within subwavelength semiconductor nano-structures, similar to the intuitive ray-optics picture of multiple total internal reflections from the periphery of the cylinder. As shown by in Ref. [81], these LMRs depend on the radius and the height of the dielectric, which allows light engineering of the nanowires so as to increase its absorption efficiency at pre-determined wavelength, e.g., to maximize absorption of sunlight spectrum for higher efficiency solar cells, or to radiate as optical antennas.

3.1.2 Whispering Gallery Modes

Infinitely long cylindrical or hexagonal NW structures can also support Whispering Gallery (WG) modes [78, 79, 84-90]. To calculate the resonant WGMs, Maxwells equations have to be solved numerically [91] taking into consideration the spectral dependence of the material of interests index of refraction. However, we can deduce a simple plane-wave model from theoretical derivations, and the relationship between resonance wavelength and the corresponding mode serial number N can be obtained [92]. The WG modes can also reflect and confine light in the (subwavelength) nanostructure by total internal reflection from the curvature of the structure boundaries. However, a light wave can interfere with itself only when having completed one full circulation within the resonator, which means only the light with one or multiple wavelengths are allowed to perform multiple circulations generating a standing wave. Figure 2 from reference 85 shows near-field intensity patterns of low-order TM polarized hexagonal WGMs for n=1 and refractive index =2.1. Each mode pattern is labeled by its respective mode number m (lower right number) and its symmetry class (upper right

symbol). For comparison, four mode patterns of the circular cavity are given in the upper left and lower right together with their angular mode number. We again observe the radial spatial dependence of light intensity. Furthermore, the low order WG modes of hexagonal NWs are essentially similar to the cylindrical ones, but for higher order modes additional features will arise on the facets of the hexagonal NWs [85]. Simulation results also show little difference between WG mode and Leaky modes in lower order modes for both hexagonal and cylindrical structures. As with the LMR, the resonant WG modes have been used as the basis for a precise theoretical explanation of the enhanced optical behavior of hexagonal NWs, such as enhanced light absorption [81, 93-96] and emission [78, 97-99]. Furthermore, these numerical solutions have lead to reproduction of experimental resonance spectra, e.g., polarization-resolved micro-photoluminescence (-PL) and cathodeluminescence (CL) spectroscopy.

3.1.3 Fabry-Perot Resonant Mode

The above analysis and results apply to long structures, hence, provide two-dimensional radial modes, independent of the NW axis. However, light confinement has strong axial dependence, necessitating three-dimensional analysis of the cavity modes. FDTD simulation in 3D are used to identify the axial dependence of resonant modes in these nano-structures, revealing modes which are volumetric in nature. Fabry-Perot (FP) modes have been analyzed for sub-microcavity, or nano-cavity, NWs with cylindrical or hexagonal structures, specifically in order to determine the axial dependence of the resonance modes [100]. At least two mirrors are needed to construct the reflection structure inside the cavity, whether they are the top and bottom ends, i.e., the air and substrate interfaces with the nanowire, or any of the two opposite facets along the nanowire axis. For subwavelength structures, the longitudinal WG modes have high scattering losses due to diffraction, and axial FP waveguide modes will dominate [90]. However, due to small difference of the refractive index between the substrate and the nanowire dielectric, the existence of the FP mode will only be valid if the nanowire has relatively large radii, e.g., larger than 200 nm [101]. Under these conditions, besides the top and bottom ends, the lateral facets of nanowire can also be treated as two parallel

slabs, and with the dielectric in between, it can support the FP mode with mode spacing inversely related to the nanowire length. An application of this analysis is in the design of NW lasers, since the optical cavity modes are observed at threshold for lasing, and have been investigated for both optical and electrical pumped cases [102, 103]. As a results the FP resonance mode based nanoscale lasers are not only capable of covering a wide spectral regions, but can also can be integrated as single or multi-color laser source arrays in silicon based photonic integrated circuit or microelectronic devices [102,103]. However, the FP modes supported by the nano-cavity structure have relatively small quality factor due to the small difference of the refractive indices of the substrate and the NWs. In order to address this issue, Bragg gratings can be produced at the NW ends, alternatively, NWs can be placed on metal substrates in order to increase the FP resonance peak intensity by more than one order of magnitude compared to those on Si substrates [104].

3.1.4 Helical Resonance Modes

Nano needles of III-V material grown on heterogeneous substrates are optoelectronic devices which have shown interesting optical behavior, including lasing, at room temperature [105]. Figure 3 (A) shows SEM image of a nano-laser grown on silicon substrate that has subwavelength dimensions on all sides. Analysis of light propagation introduced by shows that unlike the traditional WG mode that lack vertical structure, there is net propagation in axial direction in these structures which leads to volumetric resonant modes which are termed helical mode resonances [105]. The schematic Fig. 3(B) suggests a helical ray path with nearly total internal reflection at the nanopillar-silicon interface due to the glancing angle of incidence from the hexagonal facets of the nano-laser shown in Fig. 3(A). As such, the faceted shape of the structure affects the optical cavity properties. FDTD-simulated field profile shows a hexagonal WG-like mode pattern in the transverseplane as in Fig. 3 (C), which arises from strong azimuthal components of helical modes. Figure 3 (D) shows first-order and higher-order standing waves axial variation. The radial mode number (first number, m) describes the transverse field pattern for WG modes, and the axial mode number (second number, n) describes the axial standing wave as is the case for Fabry-Perot resonances. It is seen that

light or optical field can be well confined in the nanostructure even with low index contrast at the dielectric interface thus producing the nano-resonators needed for lasing. Although the quality (Q) factors of such nanostructure are usually not large, these helically propagating cavity modes, provide an optical feedback mechanism without the sophisticated mirror structures of the vertical cavity surface emitting lasers (VCSELs). Additionally, since the nanowires are heteroepitaxially grown on different substrates, they enable heterogeneous integration of photonic emitters and silicon based computational circuitry. Whereas traditional FP modes are inhibited by the interface between semiconductor nanostructure and the silicon substrate, such unique optical structures have been proposed as an avenue for engineering and integrating on-chip nanophotonic devices.

3.2 Volumetric Modes

The diameter of the nanostructures which can support the helical resonance modes is near the Rayleigh limit, around the boundary of the validity of ray-optics. FDTD analysis can be applied to deeper subwavelength structure in order to identify the cavity modes which are by nature volumetric, i.e., axially dependent. Figure 4 shows simulation results for various diameters of hexagonal structure of 1 m length. Incident radiation with 532 nm wavelength is nearly parallel to the wire axis and different modes are displayed for different radii. Top row shows radial spatial dependence at the middle of the wire axis, and the bottom row shows the axial dependence. Top row results are similar to Figures 1-2, and the bottom row shows that the light can be confined in volumetric resonance mode in both transverse plane and longitudinal plane even with sub-wavelength diameter of these hexagonal NWs. Unlike helical modes, the explanation of resonance need not rely on an intuitive ray-optics description based on the grazing angle of incident light, but shows similar results in how the deep subwavelength structures can confine the light and produce a resonant cavity without having sophisticated mirrors at the end facets. In this respect nano-cavities of as-grown nanowires outperform microcavities of VCSELs.

3.2.1 Nanocavity Geometry Dipendence

3.2.2 Light Engineering of Nanocavities

Dependence of the resonant modes on the cavity geometry offers an important degree of freedom to engineer a cavity for particular optical properties. Figure 6 shows the dependence of three volumetric TM resonant modes excitation wavelengths with radius. In this spectral range, only lower TM modes can be excited with smaller radii, e.g., r = 40 nm and 60 nm, however, as the radius increases, higher order modes can be excited, and the optical power corresponding to the lower order modes will be reduced. We observe redshift of these volumetric TM modes with increasing NW radius. Also, the wavelength variation of TM1n mode is much larger compared to TM2n and TM3n modes. These observations demonstrate the feasibility to engineer the volumetric mode at certain wavelength, i.e., allow us to optimize absorption or emission at a desired frequency or certain incident optical power by controlling the radius and/or length of a NW thus providing the ability to engineer the absorption spectrum in order to match desired properties.

iThe dependence of the resonant modes on NW radius also suggests the interesting possibility of having tapered structures which can support more than one resonant mode, thus be able to optimize the spectrum of interest. The metalorganic vapor phase epitaxy (MOVPE) or vapor liquid solid (VLS) growth methods are readily capable of forming nanowires with tapered sidewalls. The resultant cavity, however, does not support the superposition of the modes present in cylindrical structures of the same diameter; in fact tapered sidewalls have been identified as the primary loss mechanism for these sub-wavelength cavities. The effect of tapering has been studied for nanopillars that were grown on a silicon substrate with average 5 angles between opposite sidewalls; vertical field profiles for , and modes are shown in Fig. 7 [105]. The modes are primarily confined at the base, and become less resonant as they propagate upwards with decreasing of the radius at top. Higher-order axial modes generally have lower quality factor. Physically, the stronger Fabry-Perot characteristic of higher-order axial modes means that their effective longitudinal wave-vector components become stronger, causing larger penetration and loss into the substrate. Nevertheless, from

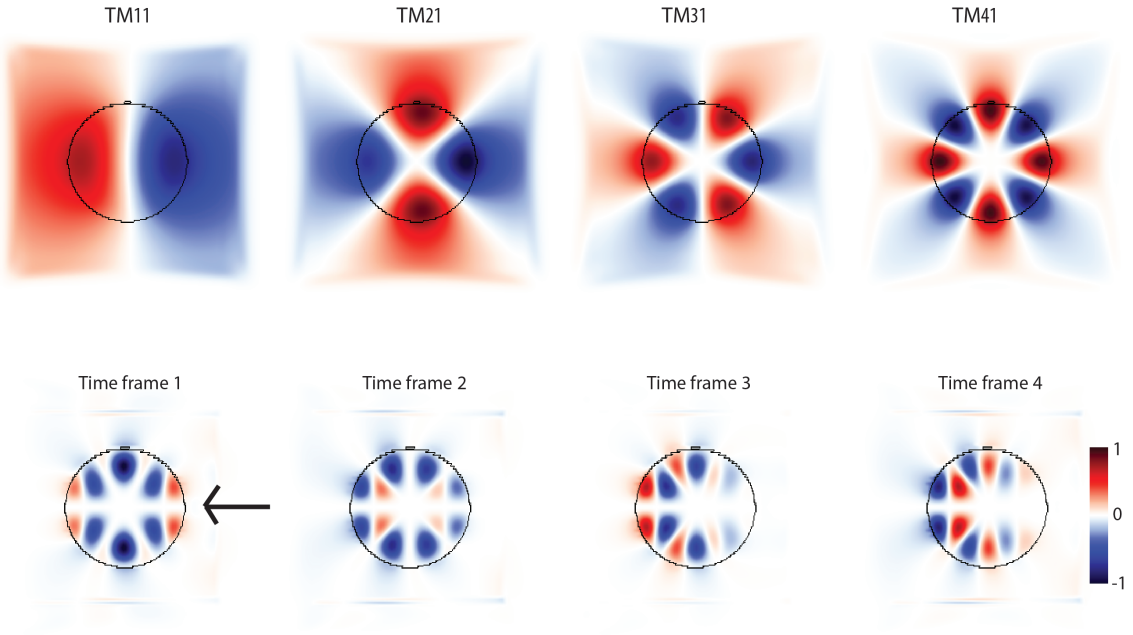

Figure 3.1 Cylindrical Nanowire Ez with different Mode number

a different perspective, multi-mode resonances can be achieved within certain wavelength range by controlling the tapering angle in order to form small varying radius along the nanostructure axial direction. One can also red- or blue-shift the resonance peaks, since these volumetric resonance modes are dependent on transverse dimensions. Thus, intentioned tapering offers an alternative way to engineering the multi-mode resonances and finer tunability of these resonance peaks.

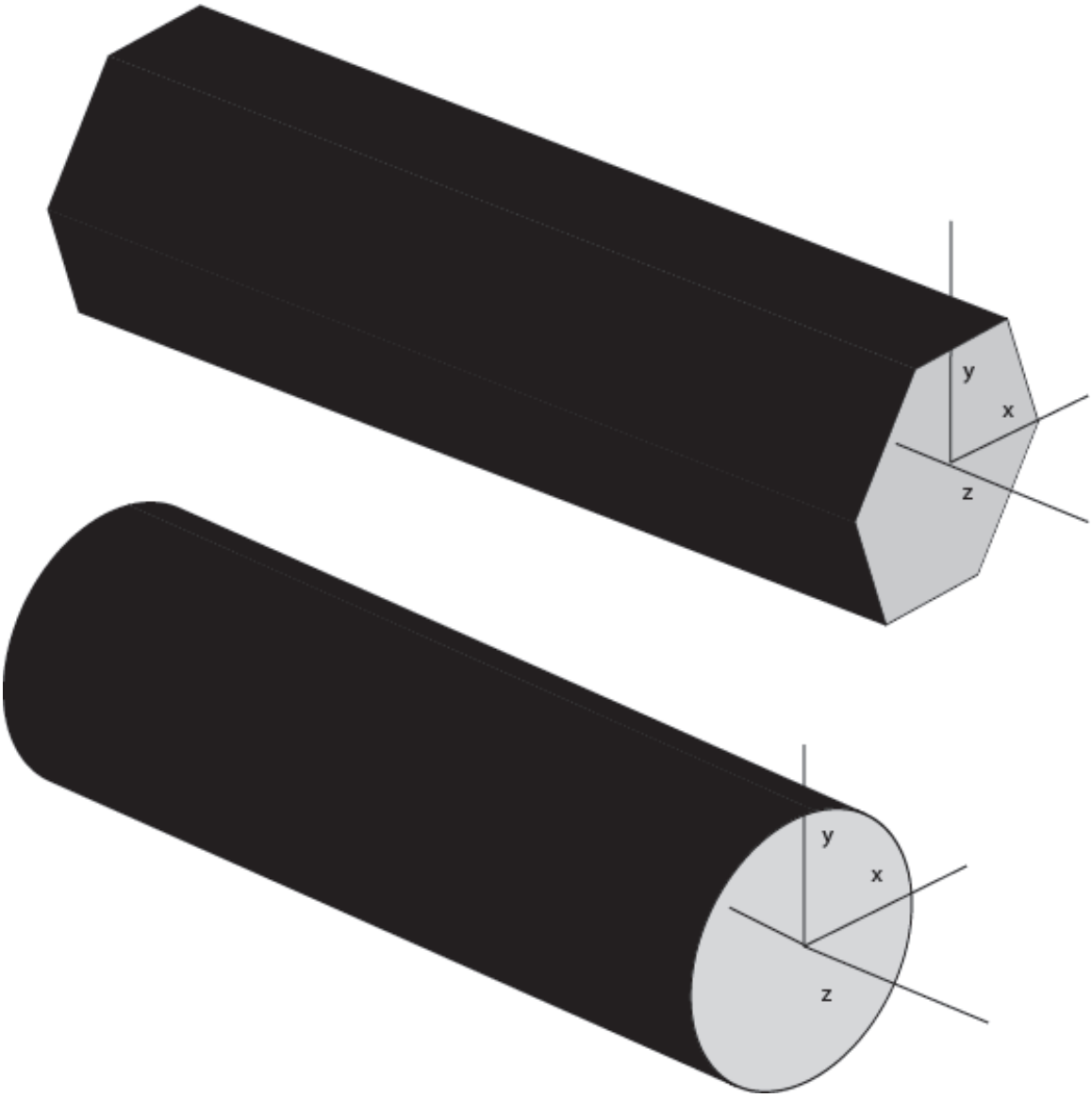

Figure 3.2 Simulation Schematic for Cylindrical and Hexagonal Nanowires

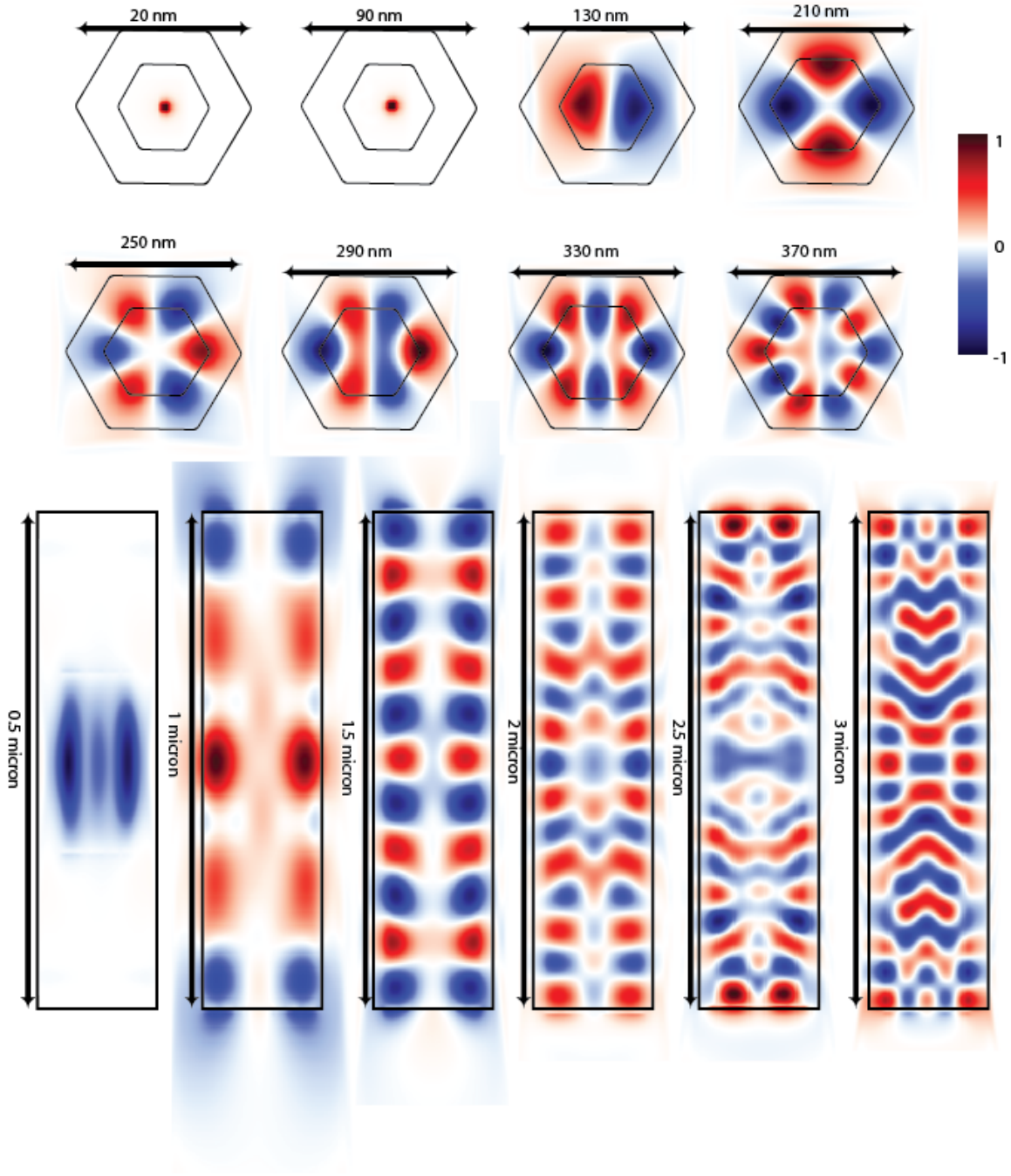

Figure 3.3 Geometric Dependence TM radius variation for different Radius and Diameters

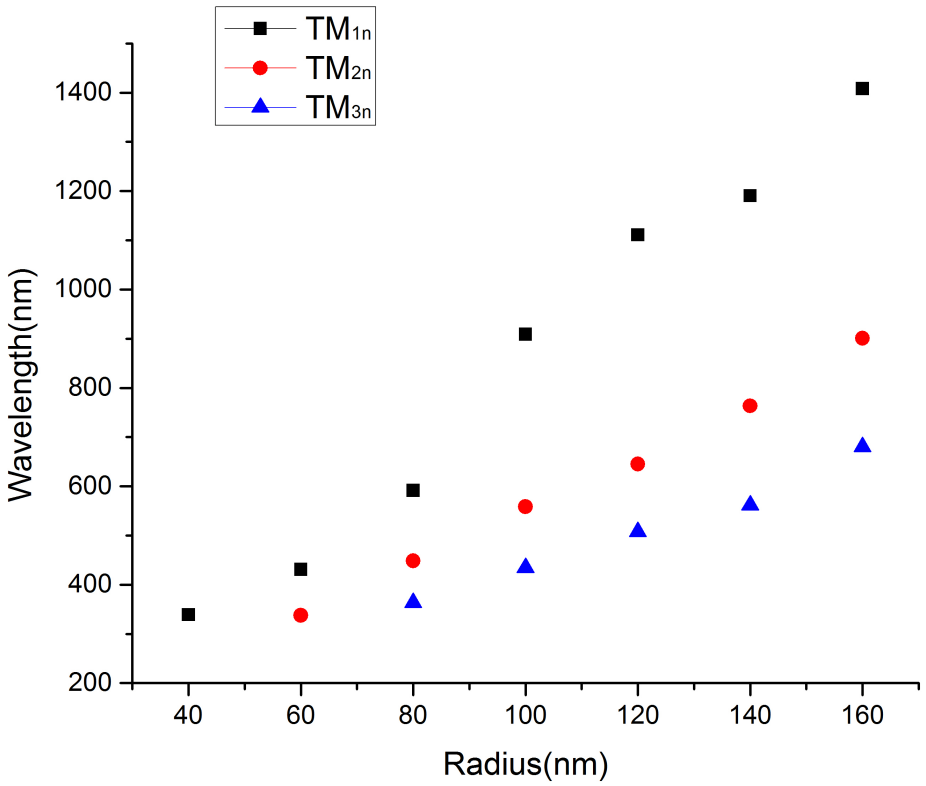

Figure 3.4 Geometric Dependence and Engineering Light with Radius

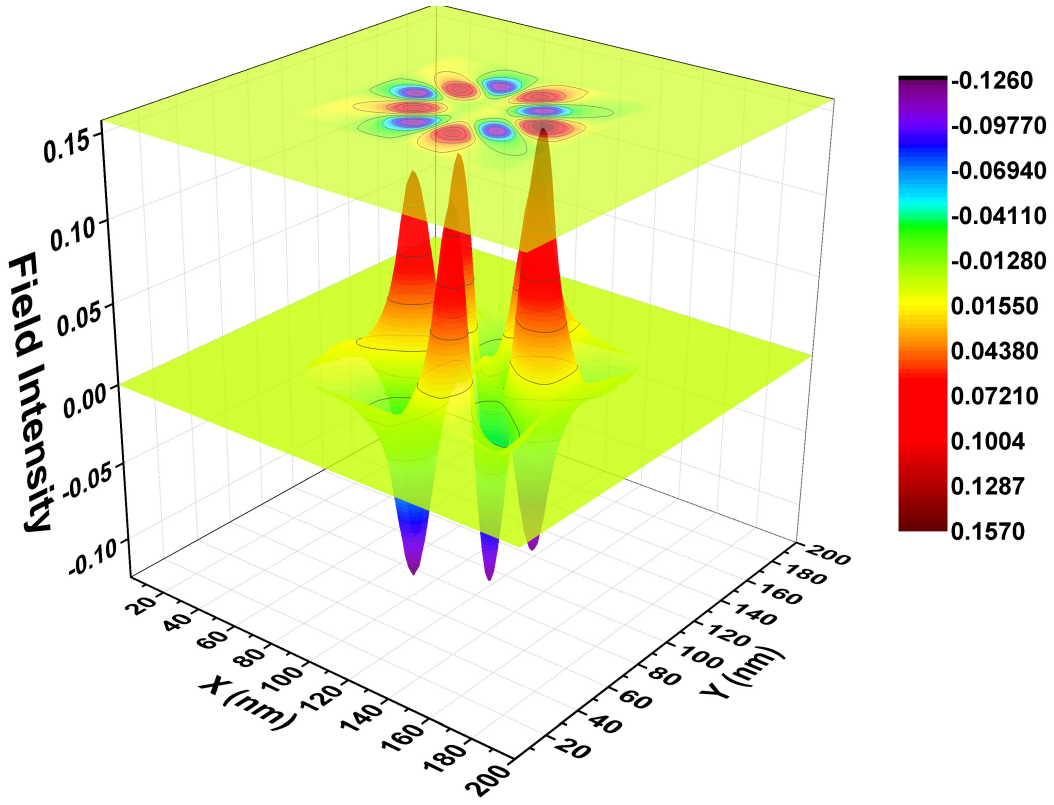

Figure 3.5 3D view of Photon Distribution

CHAPTER 4

REDUCED ELECTRONIC DENSITY DISTRIBUTION

4.1 Self-consistent Poisson-Schrodinger Solver

4.2 Electronic Distribution in Nanowires

Figure 8 (C) shows the FDTD-simulated electric field density of a hexagonal nanowire at y cross section (top) and x cross section (bottom). The photon energy of this mode shown as the insets of Fig. 8(C) is concentrated primarily along the 6 corners and secondarily along the facets with little light in the 3D core of GaAs. Hence, we suggest that the fortuitous spatial overlap of the resonant optical modes on reduced dimensional electronic wavefunctions plays a significant role in the remarkable optoelectronic properties of core-shell nanowires. Restated, the superposition of the photon modes on reduced electronic states that form on the facets and vortices of the hexagonal CSNWs strongly enhances both upward and downward transition rates. Thus, the reduced dimensionality transition rate distinguishes the core-shell nanostructure from the optically equivalent structures of Fig. 6 due to its significantly modified rate management. These nanostructures are not only excellent optical cavities, but despite their large size also provide the right reduced dimensional electronic structures which enhance optoelectronic interactions. It should be noted the present analysis is for direct optical transitions; although it can be extended to incorporate k-vector changes as in phonon scattering, other important factors such as many-body interactions need to be included in a comprehensive analysis.

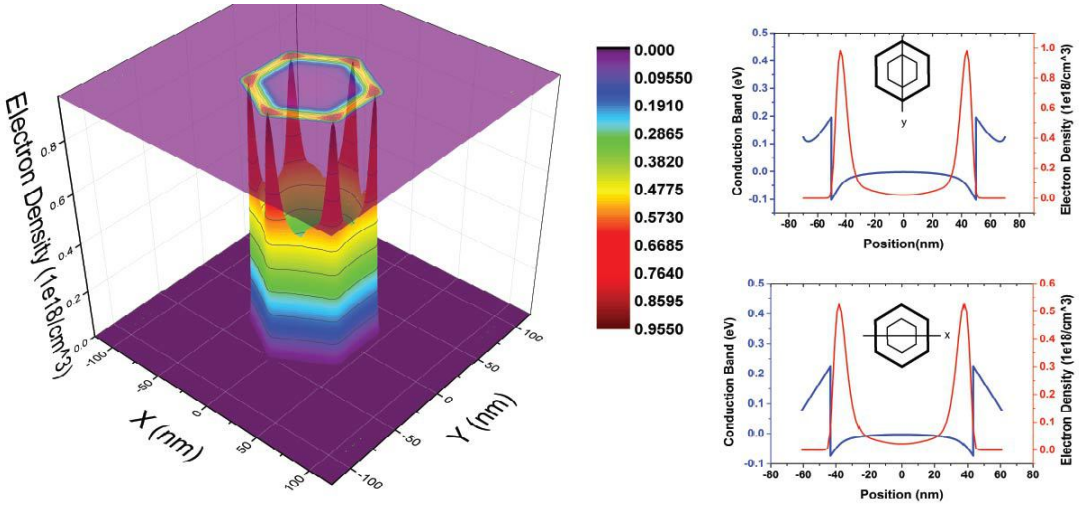

Figure 4.1 One Dimensional Electron Charge with band bending

4.2.1 Cylindrical Core-Shell Nanowire

4.2.2 Hexagonal Core-shell Nanowire

4.3 Conclusions

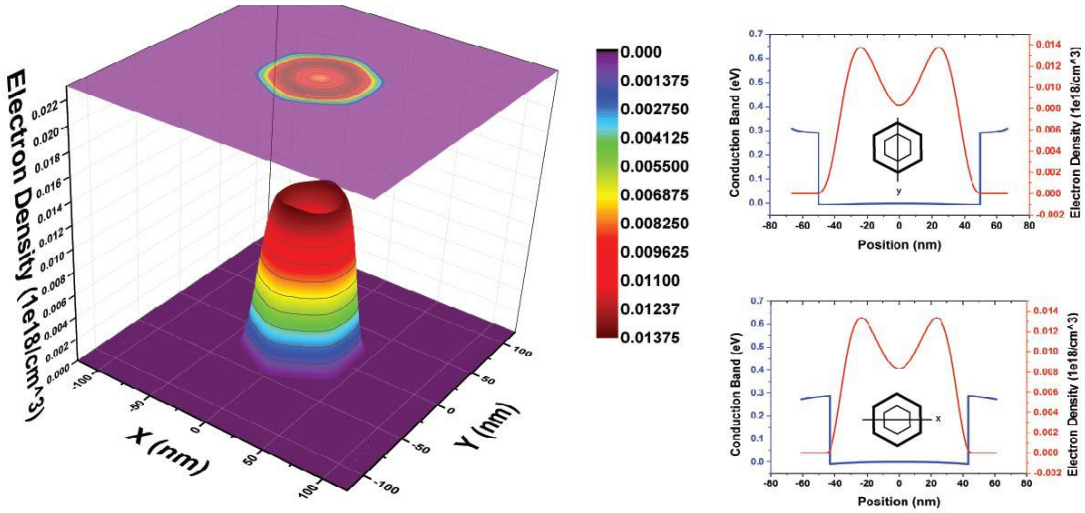

Figure 4.2 Two Dimensional Electron Charge with band bending

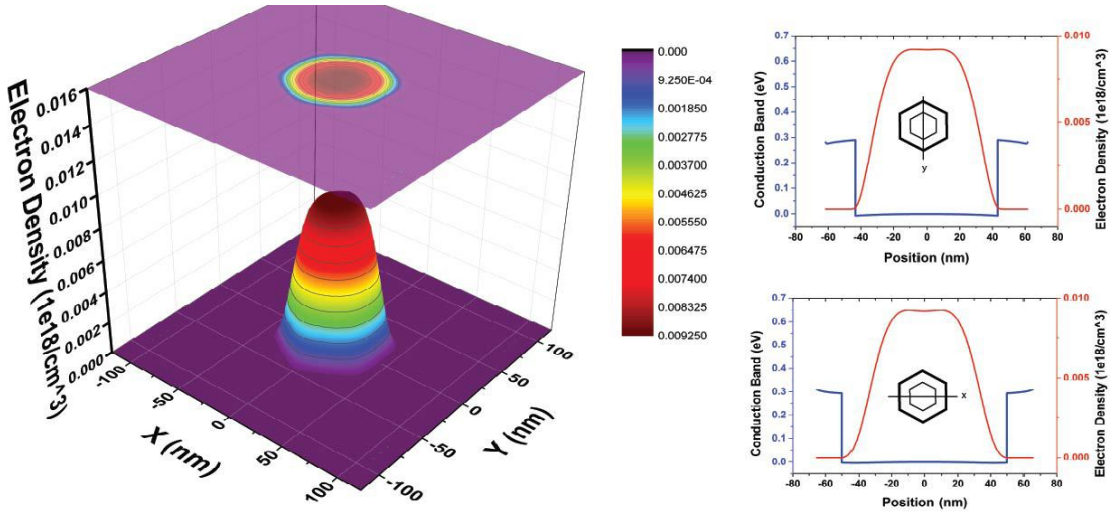

Figure 4.3 Three Dimensional Electron Charge with band bending

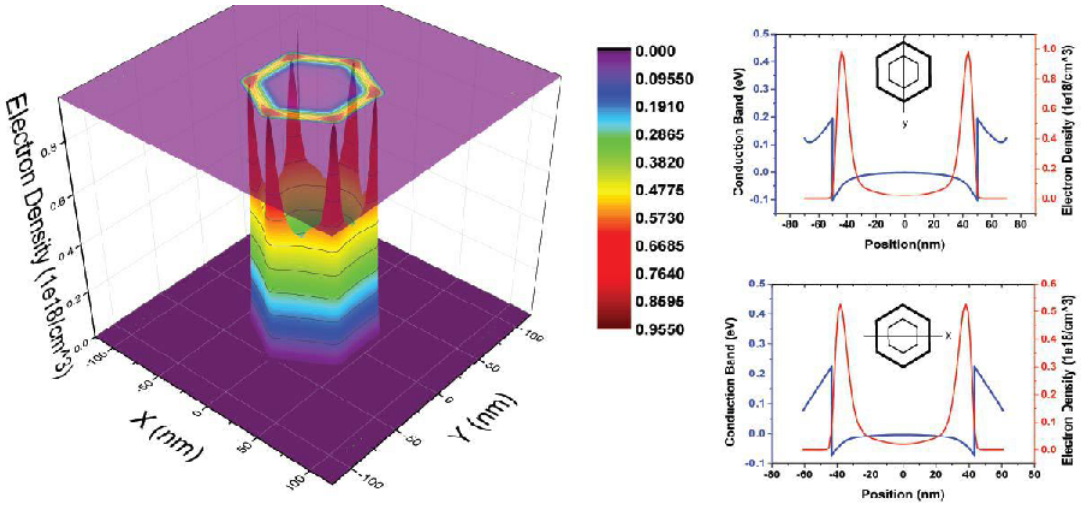

Figure 4.4 Photon Charge Distribution

CHAPTER 5

DIMENSIONAL DEPENDENCE OF OPTICAL TRANSITION RATES

5.1 Time-dependent Perturbation Theory

5.1.1

5.2 Upward and Downward Transition Rates

5.3 Contributing Factors

5.3.1 Overlap Integral

5.3.2 Oscillator Strength

5.3.3 Joint Optical Density of States

The preceding theory of gain involving Fermi's Golden Rule considers each electron in isolation as it interacts with the electromagnetic field. In other words, we have used a single-particle theory to obtain the gain spectrum. In reality, there is a large density of both electrons and holes present in the system. The mutual interactions between these particles are generally referred to as many-body effects. These effects included lineshape broadening, which is related to collisions between particles and/or phonons in the crystal. In addition to this important effect, there are two other significant consequences of many-body effects: exciton states and bandgap shrinkage. Exciton states exsit primarily at low carrier densityies and low temperatures, where bandgap shrinkage becomes noticeable at high carrier densities.

Under conditions of low carrier density and low temperature, it is possible for an electron and hole

to orbit each othere for an extended period of time, forming what is referred to as an exciton pair. Such exciton pairs have a binding energy associated with them that is euqal to the energy required to separate the electron and hole. As a rsult, electrons that are elevated from the valence band to one of these exciton states will absorb radiation at energies equal to the bandgap less the binding energy (the bandgap will appear to be red-shifted). More significatnly however, the overlap integral (and hence the matrix element) of these two-particle states can be quite large. As a result, band-to-exciton transitions tend to dominate the absorption spectrum. However, exciton states are limited to states near $k = 0$, and hence band-to-exciton transitions are clustered at the band edge (or subbabdn edge). The overall effect is the qppearance of very strong absorption peaks near the subband edges in quantum-well materials, and near the band edge in bulk material. Exciton absorption peaks are clearly visible in quantum wells at room temperature for a typical GaAs QW. The first two steps in the "staircase" absorption spectrum predicted from the density of states. However, the exciton peaks riding on top of the steps, particularly the n = 1 peaks, dominate the absorption spectrum. Each observed exciton peak corresponds to one of the subband transitions.

The second many-body effect occurs at high carrier densities, where the charges actually screen out the atomic attactive forces. With a weaker effective atomic potential, the single-atom electron wavefunctions of interest become less localized and the nearest-neighbor electron everlap becomes higher. The large overlap increases the width of the energy bands (δE is larger), reducing the gap between bands. Although this description is only qualitative, it does reveal that the bandgap should shrink with increasing carrier density. It can also be argued theoretically that the badgap shrinkage is inversely related to the average spacing between carriers, or (the closer the carriers are, the more their own Coulomb potentials screen out the atomic potential). In bulk material, the average volume occupied by one carrier is inversely related to the carrier density. The net effect of bandgap shrinkage is that as carrier density increases, the entire gain spectrum redshifts by a noticeable amount. In principle, the shift is accompanied by a slight distortion. (i.e, reshaping and enhancement) of the spectrum.

CHAPTER 6

MODELING LASING THRESHOLD

6.1 History of Semiconductor Lasers

As we know, semiconductor lasers are important optoelectric devices ofr optical communication systems. They are essential components for building optical communication systems. There are intensive research results and achievements from beginning. In 1917, Einstein predicted the existence of spontaneous and stimulated emission by which an atom can emit radiation. The first semiconductor lasers were fabricated in 1962 using homojuncations. These lasers had high threshold current density (19000/A/cm2) and operated at cryogenic temperatures. The concept of heterojuntion semiconductor lasers was realized in 1969 1970 with a low threshold current density (1600 A/cm2) operating at room temperature. These double-heterostructure diode lasers provide both carrier and optical confinements, which imporve the efficiency for stimulated emission. The concept of quantum well structures for semicondcutor lasers was proposed and realized experimentally in the late 1970s. The threshold current density was reduced to about 500 A/cm, which improved the laser performance significantly.

6.2 Principle of Semiconductor Lasers

As we know, the semiconductor laser (or laser diode) in its simplest form is a p-n junction of a single crystal of semiconductor material arranged in a cavity, as shown in . The type and configuration of the material used to determine the optical characteristics of the laser diode emission. Like others in various oscillators or wave sources, the fundamental elements in the semiconductor lasers are

the following three elements: semiconductor band structure (population inversion to provide gain mechanism), current injection and P-N junction (external pumping to make gain sustainable) and reflector of cavity (feedback to provide coherence). The most common semiconductor lasers are including Fabry-Perot(FP) or distributed feedback (DFB)/distributed Bragg reflector (DBR)

6.2.1 Absorption of Light

The light and matter interaction includes absorption, spontaneous emission and stimulated emission, we first discuss the absorption of light by introducing the absorption coeffiecient. This is the absorption rate without considering the occupation factors.

Based on the following equations for different dimensionality.

$$\begin{aligned} \alpha_{3D}(\hbar\omega) =& C_0|\hat{e}\cdot\mathbf{p_{cv}}|^{\mathbf{2}}(f_v - f_c) \\ & \frac{1}{2\pi^2}(\frac{2m_r^*}{\hbar^2})^{3/2}(\hbar\omega - E_g)^{1/2}, \\ & C_0 = \frac{\pi e^2}{n_r\epsilon_0 c m_0^2\omega}, \end{aligned} \tag{6.1}$$

$$\begin{aligned} \alpha_{2D}(\hbar\omega) &= C_0|\hat{e}\cdot\mathbf{p_{cv}}|^{\mathbf{2}}\frac{m_r^*}{\pi\hbar^2 L_z}, \\ \alpha_{1D}(\hbar\omega) &= C_0|\hat{e}\cdot\mathbf{p_{cv}}|^{\mathbf{2}}\frac{(m_r^*)^{3/2}}{\pi\hbar m_e^* L_x L_y}\frac{1}{\sqrt{(\hbar\omega - E_g)}}, \end{aligned} \tag{6.2}$$

The split plots of absorption coefficient for different dimensionality as in Fig. 6.1. Noted the unique shapes of density of states.

Then the overlay plot with multiple y axis as in Fig. 6.2 and the different scales indicating the enhancement factor for 1D is 35(need to be verified) compared to 3D.

6.2.2 Optical Gain

Following the treatments of Appendix 3, we can derive the gain spectrum for 3D, 2D and 1D with consideration of occupation factor by calculating the Fermi levels.

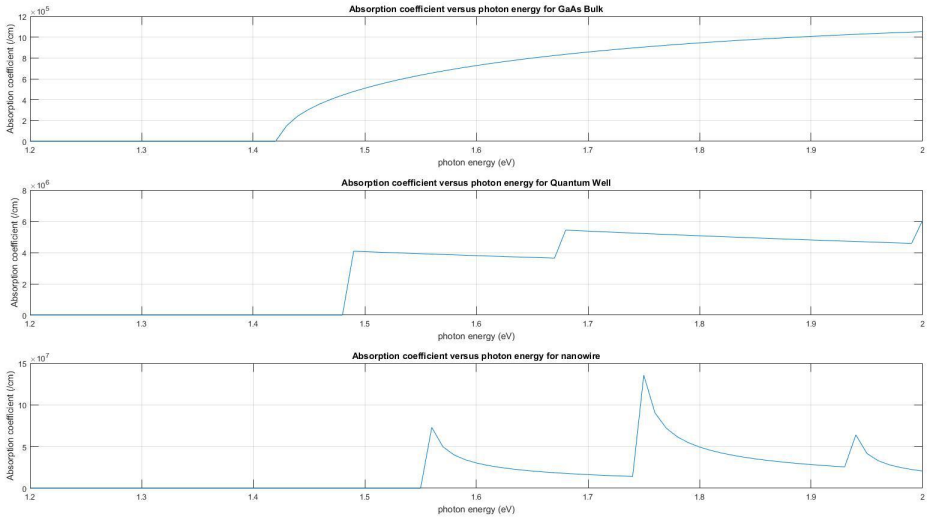

Figure 6.1 Absorption Coefficient versus Photon Energy for 1D 2D and 3D with split plot

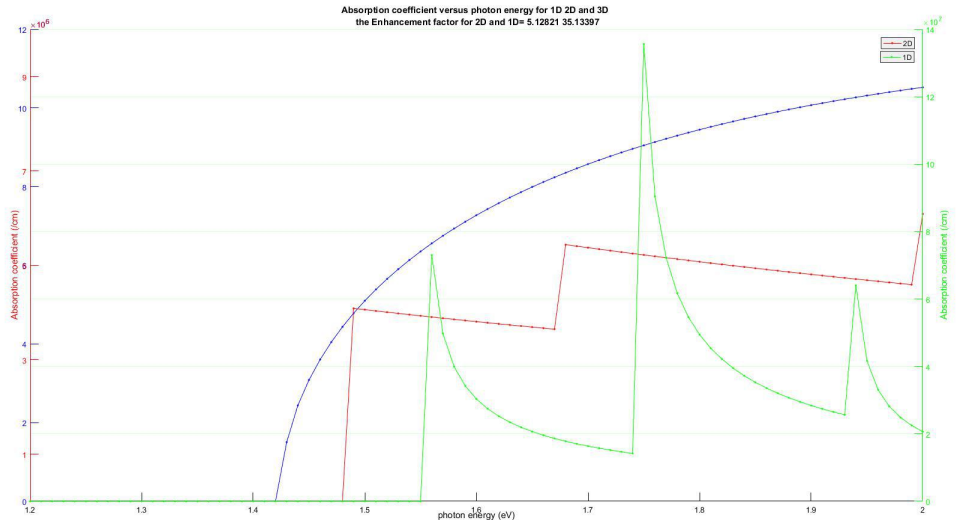

Figure 6.2 Absorption Coefficient versus Photon Energy for 1D 2D and 3D

$$
\begin{aligned}
g_{3D}(\xi) &= \frac{\sqrt{2}e^2 {m_r^*}^{3/2} p_{cv}^2}{3\pi n_r \epsilon_0 {m_0}^2 C\hbar^2 \xi}\sqrt{(\xi-\xi_g)}(f_n(\xi_2)-f_p(\xi_1)),\\
g_{2D}(\xi) &= \frac{e^2 m_r^* p_{cv}^2}{3n_r \epsilon_0 {m_0}^2 C\hbar L_z \xi}(f_n(\xi_2)-f_p(\xi_1)),\\
g_{1D}(\xi) &= \frac{e^2 {m_r^*}^{3/2} p_{cv}^2}{3n_r \epsilon_0 {m_0}^2 C\xi L_x L_y}\frac{1}{\sqrt{(\xi-\xi_g)}}(f_n(\xi_2)-f_p(\xi_1)),
\end{aligned}
\tag{6.3}
$$

Now we can plot the gain spectrum respect to photon energy for 3D, 2D and 1D in the figure below. As we can see, the gain spectrums follow the unique shapes of density of states. The fourth figure is the maximum gain versus electron carrier concentration varing from $3\times10^{18}(cm^{-3})$ to $3\times10^{19}(cm^{-3})$. Using parameters $N_{tr} = 2\times10^{18}cm^{-3}$, $N_s = 4\times10^{18}cm^{-3}$, and $g_0 = 6.11\times10^5 cm^{-1}$, we fit the curve in Fig. 6.3 to build a logarithmic gain model of the form for 3D case:

$$
g(N) = g_0 \ln\left(\frac{N+N_s}{N_{tr}+N_s}\right) \tag{6.4}
$$

where N_s is a shift to force the natural logrithm to be finite at $N=0$ such that the gain equals the umpumped absorption due to the band-to-band transitions, N_{tr} is the transparency carrier density, and g_0 is the gain coefficient. N_{tr} and g_0 will be different for different dimensionality.

After fitting the curve in Fig. 6.4, we can calculate the threshold carrier density is $N_{th} = 4.533\times10^{18}cm^{-3}$. Then plotting the spontaneous emission rate with respect to the threshold carrier density N_{th} for 3D, 2D and 1D as following:

$$
\begin{aligned}
r_{3D}^{\text{spon}}(\xi) &= \frac{n_r e^2 \xi p_{cv}^2}{\pi\epsilon_0 {m_0}^2 C^3\hbar^2}\frac{{m_r^*}^{3/2}}{2\pi^2\hbar^3}\sqrt{(\xi-\xi_g)}f_n(\xi_2)(1-f_p(\xi_1)),\\
r_{2D}^{\text{spon}}(\xi) &= \frac{n_r e^2 \xi p_{cv}^2}{\pi\epsilon_0 {m_0}^2 C^3\hbar^2}\frac{m_r^*}{\pi\hbar^2 L_z}f_n(\xi_2)(1-f_p(\xi_1)),\\
r_{1D}^{\text{spon}}(\xi) &= \frac{n_r e^2 \xi p_{cv}^2}{\pi\epsilon_0 {m_0}^2 C^3\hbar^2}\frac{{m_r^*}^{3/2}}{\pi\hbar m_e^* L_x L_y}\frac{1}{\sqrt{(\xi-\xi_g)}}f_n(\xi_2)(1-f_p(\xi_1)),
\end{aligned}
\tag{6.5}
$$

Integraing over all the photn energy spectrum, we have $R_{sp} = \int_\xi r_{sp} d\xi$ for different dimensionality,

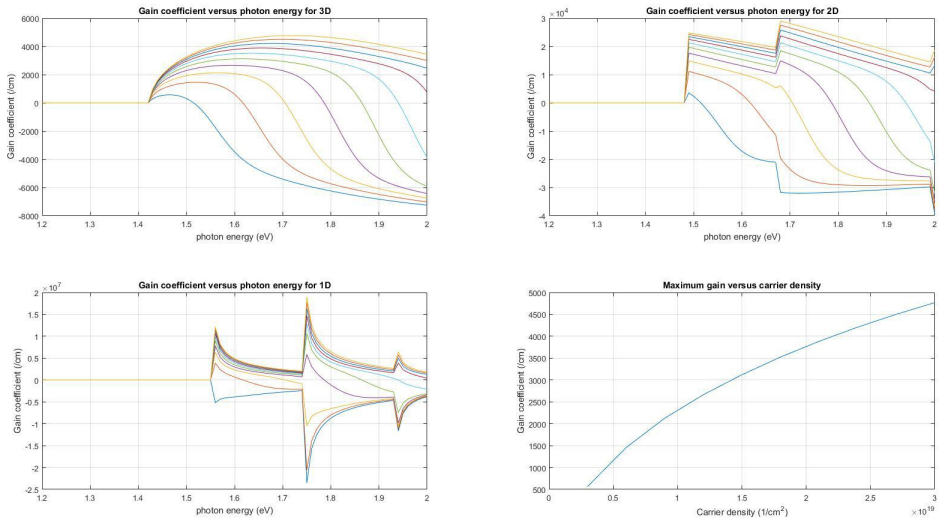

Figure 6.3 Gain Coefficient versus Photon Energy for 1D 2D and 3D

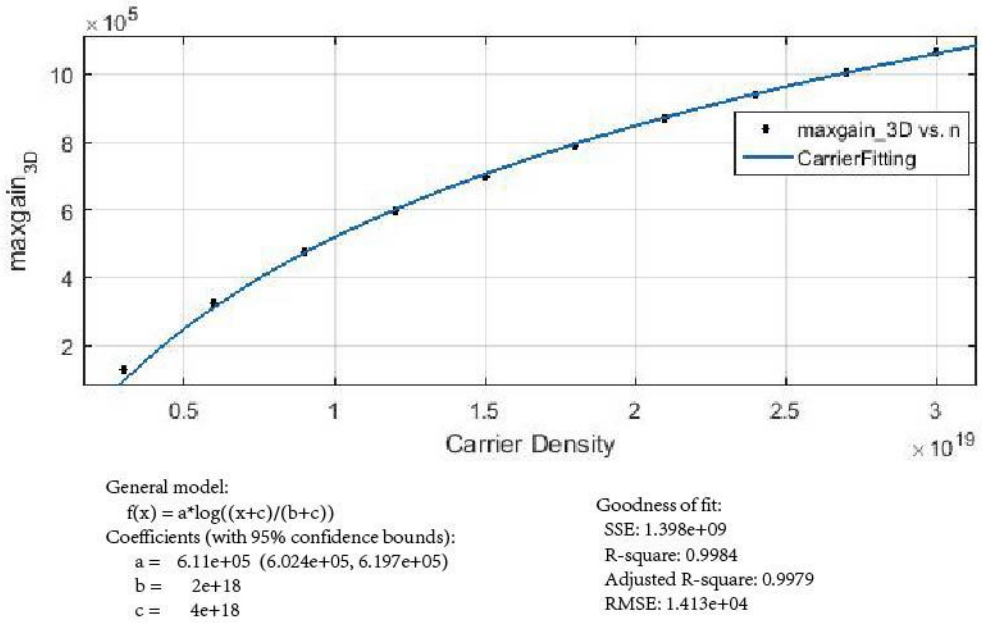

Figure 6.4 Gain Model Fitting

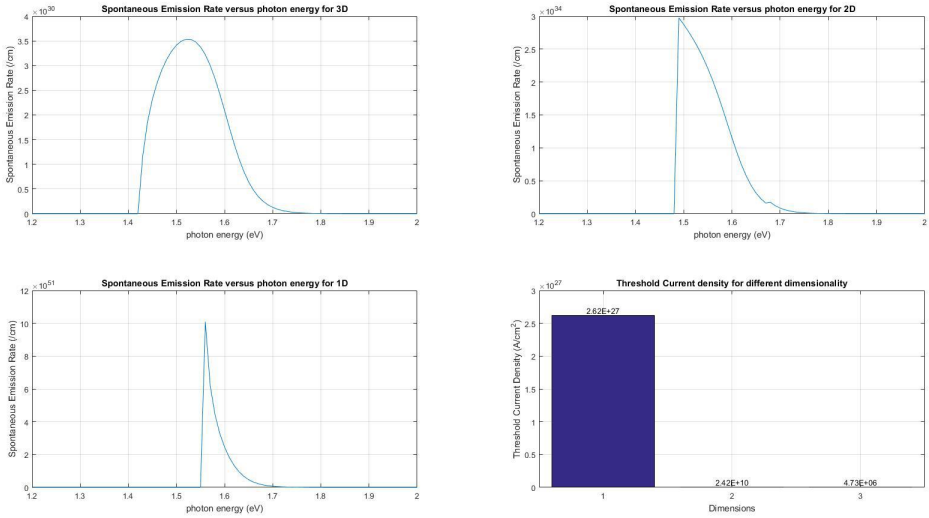

Figure 6.5 Spontaneous Emission Rate versus Photon Energy for 1D 2D and 3D

then the threshold current density can be simply caluclated as: $J_{th} = qdR_{sp}|_{N_{th}}$ and plotted in the fourth part of Fig. 6.5. The threshold current for 3D is $2.62\times10^{27}(A/cm^2)$, 2D is $2.42\times10^{10}(A/cm^2)$, and 1D case is $4.73 \times 10^6(A/cm^2)$. The threshold current density needed for lower-dimensional structure is greatly reduced.

Next, we can do dynamic analysis of laser modal and replace the threshold current density to threshold pumping power. And verify the result with the experimental data.

6.2.3 Feedback and Laser Threshold

6.3 Types of semiconductor Lasers

6.3.1 Fabry-Perot Semiconductor Lasers

The Fabry-Perot(FP) laser is conceptually just an LED with a pair of end mirrors or facets. The mirrors are needed to create the right conditions for lasing to occur. The lasing medium can only amplify (undergo stimulated emission) over a fairly narrow range because of the characteristics of the material it is made from . A typical gain curve is illustrated on the left-hand.

6.3.2 Grating-Based semiconductor Lasers

6.3.3 Vertical-Cavity Surface-Emitting Lasers

As seen, light in the VCSEL propagates vertically with DBR mirrors as the nature of the manufacturing process, the entire round-trip of the VCSEL is much shorter than that of with the edge-emitting lasers. It leads to high reflectivity (around 99.9%) of DBR mirrors, in which the large number of layers are required.

One of features related to the VCSELs is the longitudianl modal stability due to its short cavity length (around order of the wavelength). A

6.3.4 Grating Surface-Emitting Lasers

6.4 Characteristics of Semiconductor Lasers

In order to understand their operation, it is necessary to know some basic performance parameters or important features of semiconductor lasers.

6.5 Basic Requrement for Design of Semiconductor Lasers

6.5.1 Spectral width and Linewidth

FP semiconductor lasers produce a range of wavelengths. This range of wavelengths is called the "spectral width" of the laser. Typically there will be around 8 "modes" and the spectral width. In order to determin exactly the spectral shape, spectral width is usually quoted as the FWHM (Full Width Half Maximun) Instead of producing a continuous range of wavelengths over their spectral width. Semiconductor lasers produce a series of "lines" at a number of discrete wavelengths. Lines themselves vary in width (in different types of lasers) very significantly. The linewidth is inversely proportional to the coherence length of the laser.

6.5.2 Operating Wavelength, Switching Time, and Modulation

6.6 Modeling of Semiconductor Lasers

From the general formulations through the rate equations ans wave equations based on the

As we know, from different aspects of the same physics of the energy conservation, there are two basic classical methods to model the operation of semiconductor lasers. The first method, which will be summarized , applies the concept of photo/electron particle exchange with the abtract optical parameters and is suitable for the FP lasers. For the DBR/DFB lasers, due to strong non-uniformities of index distribution. The interaction between electromagnetic fields and electric particles has been considered, which . Indeed, those two methods are wholly compatible with one anohter. In this project, because we focus on the FP lasers as , we employ the first method: the standard rate equation approach.

Three fundamental elements in the semiconductor lasers: semiconductor band structure, current injection, and cavity. The former two are related to the material and junction structure and the later is related to the laser structure. For semiconductor lasers, the key in the modeling is to deal with the interaction between electromagnetic fields and gain medium. The basic procedure of modeling of semiconductor lasers: Due to the complexity of the rate equation and coupling between carrier and photon density, the coupling rate equations are further solved by numerical methods such as the standing-wave approach (in frequency domain) and the traveling-wave approach (in time domain). The stading-wave approach is based on the assumption that the temporal and the spatial dependence of field distributions of the cavity odes are separable. As such, the dynamics is considered in the modal amplitudes. Consequently, the standing-wave apporach is valid only when the photon lifetime is much shorter than the characteristic time of the laser dynamics. The traveling-wave approach, on the other hand, makes no assumptions about the cavity modes. Rather, it solves the time-dependent coupled=wave equations for the forward and the backward traveling waves directly and tehrefore is valid even the laser cavity has relatively small Q-factor and/or the characteristic time of the laser dynamics is very short. Another advantage of the traveling-wave model is that it can be readily

applied to laser diodes operated with multiple cavity modes, for which the stading-wave model may have difficulty in finding the complex roots corresponding to each mode.

6.7 Laser Rate Equations

We start with the governing equations of carrier density and photon density in the active region which is governed by a dynamic process.

$$\begin{aligned} \frac{dN}{dt} &= \frac{\eta_i I}{qV} - \frac{N}{\tau} - R_{st}, \\ \frac{dN_p}{dt} &= \Gamma v_g g N_p + \Gamma \beta_{sp} R_{sp} - \frac{N_p}{\tau_p}, \end{aligned} \tag{6.6}$$

where β_{sp} is the spontaneous emission factor, defined as the percentage of the total spontaneous emission coupled into the lasing mode. And it is just the reciprocal of the number of available optical modes in the bandwidth of the spontaneous emission for uniform coupling to all modes. The g is Incremental gain per unit length.

The first term of equation 1 is the rate of injected electrons $G_{gen} = \Gamma_i I/qV$, $\Gamma_i I/q$ is the number of electrons per second being injected into the active region, where V is the volume of the active region. The rest terms are the rate of recombining of electrons per unit volume in the active region. There are several mechanisms should be considered, including a spontaneous recombination rate, R_{sp}, a nonradiative recombination rate, R_{nr}, a carrier leakage rate, R_l and a net stimulated recombination, R_{st}, including both stimulated absorption and emission. Which looks like:

$$R_{rec} = R_{sp} + R_{nr} + R_l + R_{st} \tag{6.7}$$

The above equation used input current intensity, I, for electrically injected lasing situation, however, if optical pump used as the lasing source, then we need to rewrite the governing equations.

$$\begin{aligned}\frac{dN}{dt} &= \frac{\eta_i P}{qV} - \frac{N}{\tau} - R_{st}, \\ \frac{dN_p}{dt} &= \Gamma v_g g N_p + \Gamma \beta_{sp} R_{sp} - \frac{N_p}{\tau_p},\end{aligned} \tag{6.8}$$

P is the optical pump used for exciting nano-cavity laser emission and is time-dependent of the form $P_p sech^2(\frac{1.76t}{\delta t})$, where P_p is the peak power amplitude, and δt is the time pulse width.

The cavity loss can be characterized by a photon decay constant or lifetime, τ_p, and the gain necessary to overcome losses, and thus reach threshold. By assuming steady-state conditions (i.e. $dN_p/dt = 0$), and solving for this steady-state or threshold gain, g_{th}, where the generation term equals the recombination term for photons. We assume only a small fraction of the spontaneous emission is coupled into the mode (i.e. β_{sp} is quite small), then the second term can be neglected, and we have the solution:

$$\Gamma g_{th} = \frac{1}{v_g \tau_p} =< \alpha_i > +\alpha_m \tag{6.9}$$

The product, Γg_{th}, is referred to as the threshold modal gain because it now represents the net gain required for the mode as a whole, and it is the mode as a whole that experiences the cavity loss. $< \alpha_i >$ is the average internal loss, and α_m is the mirror loss if we considered an in-plane wave laser.

$$R_{rec} = R_{sp} + R_{nr} + R_l + R_{st} \tag{6.10}$$

The first three terms on the right refer to the natural or unstimulated carrier decay processes. The fourth one, R_{st}, require the presence of photon.

Then, recognizing that $(R_{sp} + R_{nr} + R_l) = AN + BN^2 + CN^3$ depends monotonically on N, we observe from eq 2.34 that above threshold $(R_{sp} + R_{nr} + R_l)$ will also clamp at its threshold value, given by Eq 2.35. Thus, we can substitute Eq 2.35 into the carrier rate equation, eq 2.16 to obtain

a new above threshold carrier rate equations,

$$\frac{dN}{dt} = \eta_i \frac{(I - I_{th})}{qV} - v_g g N_p, \quad (I > I_{th}) \tag{6.11}$$

We also calculate a steady-state photon density above threshold where $g = g_{th}$,

$$N_p = \frac{\eta_i (I - I_{th})}{q v_g g th V} \quad (steady\ state) \tag{6.12}$$

To obtain the power out, we first construct the stored optical energy in the cavity, E_{os}, by multiplying the photon density, N_p, by the energy per photon, hv, and the cavity volume, V_p. That is $E_{os} = N_p hv V_p$. Then, we multiply this by the erngy loss rate through the mirrors, $v_g \alpha_m = \frac{1}{\tau_m}$, to get the optical power output from the mirrors,

$$P_0 = v_g \alpha_m N_p hv V_p \tag{6.13}$$

Substituting from , and using $\Gamma = V/V_p$,

$$P_0 = \eta_i (\frac{\alpha_m}{< \alpha_i > + \alpha_m}) \frac{hv}{q} (I - Ith), \quad (I > I_{th}) \tag{6.14}$$

We can get the threshold carrier density

$$N_{th} = N_{tr} e^{g_{th}/g_0 N} = N_{tr} e^{(<\alpha_i> + \alpha_m)/\Gamma g_0 N} \tag{6.15}$$

Using the polynomial fit for the recombination rates, and recognizing that for the best laser material the recombination at threshold is dominated by spontaneous recombination, we have, $I_{th} \cong$

$BN_{th}{}^2 qV/\eta_i$, Thus

$$I_{th} \cong \frac{qVBN_{tr}{}^2}{\eta_i} e^{(<\alpha_i>+\alpha_m)/\Gamma g_0 N} \tag{6.16}$$

where for most $III-V$ materials the bimolecular recombination coefficient, $B \sim 10^{-10} cm^3/s$.

Reduce the transparency value and increase the differential gain of the active materials.

It is desirable to reduce the cavity loss ($< \alpha_i > + \alpha_m$) and volume, V, in order to retaining a reasonably large confinement factor, Γ.

6.8 Wave Model of Semiconductor Lasers

6.9 Linewidth Enhancement Factor

Electrons and holes frequently interact with other carriers and with phonons, thereby changing their energy within the sub-band. Such intra-band scatter events happen about every 0.1 ps, much more often than band-to-band recombination events. Thus, scattering leads to an uncertainty of the electron energy, which can be accounted for by introducing a symmetrical linewidth broadening funtion L into the gain formula. This convolution integral means that gain at the photon energy can now receive contributions from electron transitions with, weighted by

In fact, positive gain is now possible even for photon energies slightly below the bandgap. Cauchy himself exploited such a density function in 1827, with infinitesimal scale parameter, in defining a Dirac delta function, while among physicists, it is known as the Lorentzian line shape functionL with the half-width. This function is based on the assumption that the occupation probability of an electron state decays proportionally to exp(-t/). The Fourier transformation of this exponential function into the nergy domain leads to . Gamma is the average of the broadening in the conduction and inthe valence band. The full linewidth 2gamma is related to the average intra-band scattering time

Which includes scattering events in the conduction band and valence band. For each band, linewidth

contributions from different scattering processes are adding up.

6.10 Implementations

6.10.1 Optical Modes

6.10.2 Steady State Analysis

6.10.3 Dynamic State Analysis

6.11 Simulation Results

6.11.1 Input Parameters

6.11.2 Optical Modes

6.11.3 Steady State Analysis

6.11.4 Dynamic State Analysis

CHAPTER 7

CONCLUSIONS AND FUTURE RESEARCH

As mentioned previously, communication of information, together with storage and computation form a grand challenge of the information age [2, 7]. Recently, the analysis of big data has become the engine for societal, financial, scientific, and technological endeavors. This demands an infrastructure that is capable of fast and reliable high volume data processing. Traditionally, this requirement was fulfilled by silicon technology. However, silicon-based technology has its own limitations, such as speed limit and heat dissipation problem. In order to process high volume data, we need data computation, storage and communication work as three fundamental functions of a computation cell. A monolithic nano-system may be envisioned which incorporates NWs as waveguides, detectors, photovoltaic cells, antennas, modulators, (photo)capacitors, LEDs, and lasers, .These components may be incorporated in circuit layers, such as network on chip. Different layers can communicate using NW through-silicon vias (TSVs). Similar low-power/high-performance advantages can be realized through achievement of high interconnect densities on the 2.5D Though-Si-Interposer (TSI) as reported in [114].

In conclusion, optical properties of nano-cavities were reviewed here emphasizing the analysis of resonant optical modes which depend both radially and axially on the geometries of the nanowires. This shows how such sub-wavelength structures can form optical cavities as-grown, without needing sophisticated facet mirrors. In addition, we show how the fortuitous overlap of the reduced dimensional electronic wave functions and the photonic modes is responsible for the extraordinary optoelectronic properties of core-shell nanowires. Such nano-structures have been developed on het-

erogeneous substrates, particularly silicon, and as such becoming an important component in the next generation of photonic integrated circuits which are particularly useful in meeting the grand challenge of low energy and fast speed computation.

7.1 Contributions of this dissertation

7.2 Outline of the future work

Low dimensional electron gases exsit at the heterointerfaces of core-shell nanowires (CSNWs). For example, the GaAs/AlGaAs CSNWs typically form a hexagonal structure in which six (6) pillars of 1D charge at the vortices, and six (6) sheets of 2D charge at facets are formed [1]. At the same time, nanowires (NW) have also been shown to be capable of confining light in their sub-wavelength nano-structure, supporting photonic modes, and producing resonant cavities without the need for polished end facets. We have previously shown how the electronic wave functions that are thus formed affect the optical transition rates, resulting in orders of magnitude enhancement in absorption and emission of light [ref]. Here we report on the plasmonic effects of the confined charge on the optical properties of CSNWs We report on finite difference time domain (FDTD) simulations with the aim of identifying the surface plasmon resonance modes which affect light confinement in hexagonal CSNWs, and help form a high quality factor resonant cavity. This is done by comparing regular CSNW, with a) wires covered with metal which produces surface plasmon-polaritons (SPP); b) NWs covered with metal that is sandwiched between the core and the outer, shell; and c) two-dimensional electron gas (2DEG) which embedded at the heterointerace of CSNWs. Results show that the 2DEG behaves similarly to an embedded metallic surface, allowing for highly localized light confinement in these wires without the need for vertical structures such as Bragg mirrors commonly used in vertical cavity surface emitting lasers (VCSELs). Besides affecting the cavity, the 2DEG enhances the transition rates due to the plasmon-electron interaction, facilitating not only photonic stimulated emission and lasing, but also surface plasmon amplification by stimulated emission of radiation [2].

We model the dielectric function of the two dimensional electron gas using the Drude model for

dispersive media, and extract its relevant parameters from [3]. The complex conductivity of the 2DEG is derived using the relaxation time approximation, effective reduced mass of electrons, and the density of the carriers in the gas. By substitution the complex conductivity in Drude model, we can model the 2DEG, with given plasma frequency, damping coefficient, and the oscillator strength using FDTD simulator.

The two dimensional plasma frequency is calculated as [3]: in which, is the background dielectric constant and m* is the effective mass of the electron. It is important to note that, as shown in (1), the plasma frequency of the 2DEG can be tuned with changing the carrier concentration. This tubnability distinguishes the 2DEG from other plasmonic material such as metals. The complex conductivity of the electron gas is derived as [4]:

Surface plasmon polaritons are density oscillations of electrons at the surface of a dielectric. Noble metals such as Au and Ag are considereed as the best plasmonic material candidates because of their high conductivity and low loss. The important parameters fro choosing the metals in plasmonic nanowire are the relaxation time and the plasma frequency of the metallic layer. Since silver has the smallest relaxation time, we coat a CSNW with it in order to study its effect on the NW cavity. we futhre embed Ag between the GaAs core and AlGaAs shell and compare its affect on the field profile and mode generation. Finally, we compare this configuration with a relatively dense 2DEG which is formed at the heterointerface of CSNWs. Simulation is performed using MIT's MEEP open source finite-differnce time-domain (FDTD) simulation software. For modeling the 2DEG we use data in , and for metallic layers, we used Lorentz-Drude model based on experimental data extracted from.

Figure shows the FDTD-simulated electric field profile (linear scale) in the transverse plane of (a) CSNW; (b) CSNW with silver coating; (c) CSNW with and embedded silver layer between the core and the shell; (d) CSNW with 2DEG at the hetero-interface. As shown in Fig, coating the wire with metal introduces plasmonic modes in the structure that enhance light confinement. Metal embedded betweeen the core and the shell has similar effect. Importantly, we observe that similar plasmonic features can be obtained due to the 2DEG that is embedded in CSNW.

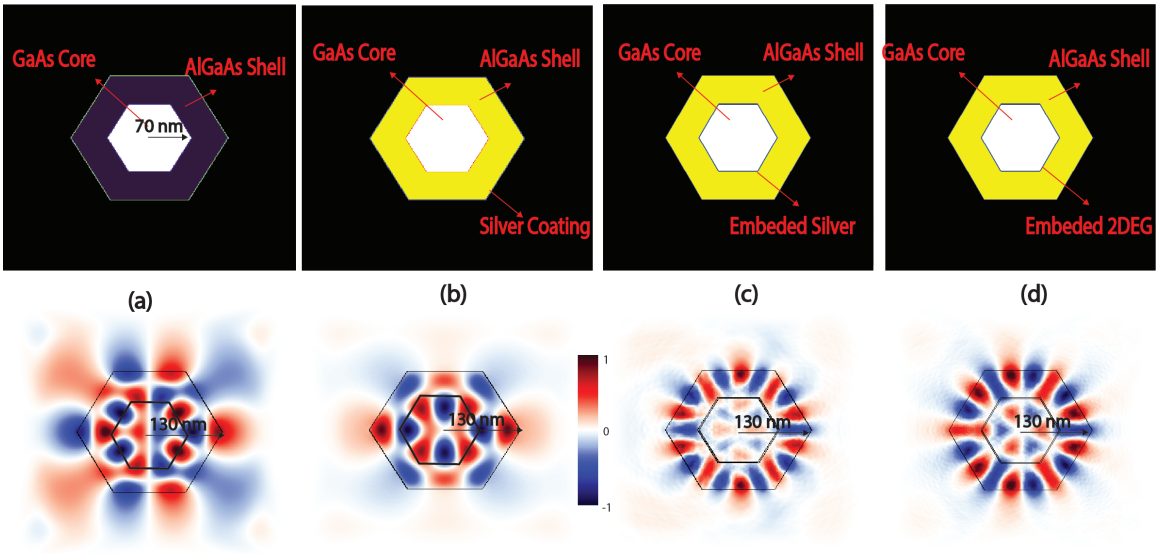

Figure 7.1 An FDTD-simulated electric field profile (linear scale) of (a) a hexagonal core-shell nanowire (CSNW), (b) photonic modes are affected by plamonic modes in a CSNW covered with silver coating, (c) CSNW with embedded silver layer between the core and the shell; (d) plasmonic and photonic modes of CSNW with embedded 2DEG show similar effects compared to embedded metal. The black boundaries represent the interface betweeen layers of the structure.

BIBLIOGRAPHY

[1] Givargizov, E. 1975, Journal of Crystal Growth, 31, 20

[2] Motohisa, J., Noborisaka, J., Takeda, J., Inari, M., & Fukui, T. 2004, Journal of Crystal Growth, 272, 180

[3] Wagner, R., & Ellis, W. 1964, Applied Physics Letters, 4, 89

APPENDIX A

TRANSITION RATES

This research project focuses on the dimensional dependence of the absorption behavior in semiconductor when interacting with light. Through time-dependent perturbation theory, we find out the transition rate and Fermis Golden Rule, then based on the light interaction Hamiltonian, time average Poynting vector and matrix element, derive the absorption coefficient for bulk semiconductor (3-dimension), quantum well (2-dimension) and quantum wire (1-dimension) structure. Finally, this report will discuss the partial confinement on the electron in the conduction band without the hole confined in the valence band situation.

The Schrdinger equation:

$$\mathcal{H}\Psi(r,t) = -\frac{\hbar}{i} frac\partial\partial t\Psi(r,t) \tag{A.1}$$

The Hamiltonian $\mathcal{H}$ can be expressed as:

$$\mathcal{H} = \mathcal{H}_0 + \mathcal{H}'(r,t) \tag{A.2}$$

where $\mathcal{H}_0$ is the unperturbed part Hamiltonian and is time-independent, $\mathcal{H}'(r,t)$ is the small perturbation.

The solution to the unperturbed part is assumed known:

$$\mathcal{H}_0\Psi_n(r,t) = -\frac{\hbar}{i}$$

$$frac\partial\partial t\Psi_n(r,t), \tag{A.3}$$

$$\frac{dN_p}{dt} = \Gamma v_g g N_p + \Gamma\beta_{sp}R_{sp} - \frac{N_p}{\tau_p},$$

The time-dependent perturbation is assumed to have the form

$$\mathcal{H} = \begin{cases} \mathcal{H}'(r)e^{-i\omega t} + \mathcal{H}'^{+}(r)e^{+\omega t}, & t \geq 0 \\ 0, & t < 0 \end{cases} \tag{A.4}$$

Expand the wave function in terms of the unperturbed solution, we find out $\Psi(r,t)$:

$$\Psi(r,t) = \sum_n a_n(t)\Phi_n(r)e^{(-iE_nt/\hbar)} \tag{A.5}$$

$|a_n(t)|^2$ gives the probability that the electron is in the state n at time t.

Substituting the expansion for Ψ into Schrdinger equation and using (II.3), we have

$$\sum_n \frac{da_n(t)}{dt}\Psi_n(r)e^{-iE_nt/\hbar} = -\frac{\hbar}{i}\sum_n \mathcal{H}'(r,t)a_n(t)\Phi_n(r)e^{(-iE_nt/\hbar)} \tag{A.6}$$

Taking the inner product with the wave function ${\Phi_m}^{\star}(r)$, and using the orthonormal property,

$$I_{hm}^{en} = \int_{-\infty}^{\infty} \Phi_n^*(z)g_m(z)\,\mathrm{d}z, \tag{A.7}$$

$$I_{hm}^{en} = \int_{-\infty}^{\infty} \Phi_n^*(z)g_m(z)\,\mathrm{d}z, \tag{A.8}$$

Therefore, the electron stays at the state i in the absence of any perturbation. The first order

solution is

If we consider the photon energy to be near resonance, either or, we find the dominant terms: The absorption coefficient is a strong function of dimensionality. The confining situation of the quantum structure will considerably affect the energy levels, the overlap function of the conduction and valance band envelope function and also the joint optical density of state. Through the derivation of the absorption coefficient, we can observe the interaction between the light and semiconductor. The next questions should address: 1. The simulation data for single nanowire abs

APPENDIX B

SEMICONDUCTOR LASER MODELING

In this section, we are trying to delve into the mechanics of how an injected current actually results in an optical output in a semiconductor heterojunction laser by providing a systematic derivation of the dc light-current characteristics. First, the rate equation for photon generation and loss in a laser cavity is developed. This shows that only a small portion of the spontaneously generated light contributes to the lasing mode. Most of it comes from the stimulated recombination of carriers. All of the carriers that are stimulated to recombine by light in a certain mode contribute more photons to that same mode. Thus, the stimulated carrier recombination/photon generation process is a gain process. We find the threshold gain for lasing which is the gain necessary to compensate for cavity losses. The threshold current is the current required to reach this gain

For electrons and holes in the active region of a diode laser, only a fraction, η_i, of injected current will contribute to the generation of carriers.We assumed the active regions that are undoped or lightly doped, so that under high injection levels, charge neutrality applies and the electron density equals the hole density (i.e., $N = P$ in the active region). Thus, we can greatly simplify our analysis by specifically tracking only the electron density, N.

We start with the governing equations of carrier density and photon density in the active region which is governed by a dynamic process.

$$\begin{aligned}\frac{dN}{dt} &= \frac{\eta_i I}{qV} - \frac{N}{\tau} - R_{st}, \\ \frac{dN_p}{dt} &= \Gamma v_g g N_p + \Gamma \beta_{sp} R_{sp} - \frac{N_p}{\tau_p},\end{aligned} \tag{B.1}$$

where β_{sp} is the spontaneous emission factor, defined as the percentage of the total spontaneous emission coupled into the lasing mode. And it is just the reciprocal of the number of available optical modes in the bandwidth of the spontaneous emission for uniform coupling to all modes. The g is Incremental gain per unit length.

The first term of equation 1 is the rate of injected electrons $G_{gen} = \Gamma_i I/qV$, $\Gamma_i I/q$ is the number of electrons per second being injected into the active region, where V is the volume of the active region. The rest terms are the rate of recombining of electrons per unit volume in the active region. There are several mechanisms should be considered, including a spontaneous recombination rate, R_{sp}, a nonradiative recombination rate, R_{nr}, a carrier leakage rate, R_l and a net stimulated recombination, R_{st}, including both stimulated absorption and emission. Which looks like:

$$R_{rec} = R_{sp} + R_{nr} + R_l + R_{st} \tag{B.2}$$

The first three terms on the right refer to the natural or unstimulated carrier decay processes. The fourth one, R_{st}, require the presence of photon.

The natural decay process can be described by a carrier lifetime, τ. In the absence of photon or a generation term, the rate equation for carrier decay is $dN/dt = -N/\tau$, where $N/\tau = R_{sp} + R_{nr} + R_l$.

The natural decay rate can also be expressed in a power series of the carrier density, N. We can also rewrite $R_{rec} = BN^2 + (AN + CN^3) + R_{st}$. Where R_{sp} BN^2 and $R_{nr} + R_l$ $(AN + cN^3)$. The coefficient B is the bimolecular recombination coefficient, and it has a magnitude, $B \sim 10^{-10} cm^3/s$ for most AlGaAs and InGaAsP alloys of interest.

When a laser is below threshold, in which the gain is insufficient to compensate for cavity losses,

the generated photons do not receive net amplification. The spontaneous photon generation rate per unit volume is exactly equal to the spontaneous electron recombination rate, R_{sp}, because an electron-hole pair will emit a photon when they recombine radiatively. Under steady-state conditions ($dN/dt = 0$), the generation rate equals the recombination rate with $R_{st} = 0$.

$$\frac{\eta_i I}{qV} = R_{sp} + R_{nr} + R_l \tag{B.3}$$

The spontaneously generated optical power, P_{sp}, is obtained by multiplying the number of photons generated per unit time per unit volume, R_{sp}, by the energy per photon, $h\upsilon$, and the volume of the active region, V.

$$P_{sp} = h\upsilon V R_{sp} = \eta_i \eta_r \frac{h\upsilon}{q} I \tag{B.4}$$

The main photon generation term above threshold is R_{st}. Electron-hole pair is stimulated to recombine, another photon is generated. But since the cavity volume occupied by photons, V_p, is usually larger than the active region volume occupied by electrons, V, the photon density generation rate will be $[V/V_p]R_{st}$, not just R_{st}. The electron-photon overlap factor, $[V/V_p]$, is generally referred to as the confinement factor, Γ.

B.1 Threshold or Steady-State Gain in Lasers

The cavity loss can be characterized by a photon decay constant or lifetime, τ_p, and the gain necessary to overcome losses, and thus reach threshold. By assuming steady-state conditions (i.e. $dN_p/dt = 0$), and solving for this steady-state or threshold gain, g_{th}, where the generation term equals the recombination term for photons. We assume only a small fraction of the spontaneous emission is coupled into the mode (i.e. β_{sp} is quite small), then the second term can be neglected,

and we have the solution:

$$\Gamma g_{th} = \frac{1}{v_g \tau_p} =< \alpha_i > +\alpha_m \tag{B.5}$$

The product, Γg_{th}, is referred to as the threshold modal gain because it now represents the net gain required for the mode as a whole, and it is the mode as a whole that experiences the cavity loss. $< \alpha_i >$ is the average internal loss, and α_m is the mirror loss if we considered an in-plane wave laser.

The optical energy of a nano-cavity laser propagates in a dielectric waveguide mode, which is confined both transversely and laterally as defined by a normalized transverse electric field profile, $U(x, y)$. In the axial direction this mode propagates as $exp^{(-j\beta z)}$, where β is the complex propagation constant, which includes any loss or gain. Thus, the time- and space-varying electric field can be written as

$$\xi = \hat{e}_y E_0 U(x, y) e^{j(\omega t - \beta z)} \tag{B.6}$$

where $\hat{e}_y$ is the unit vector indicating TE polarization and E_0 is the magnitude of the field. The complex propagation constant, β, includes the incremental transverse modal gain, $< g >_{xy}$ and internal modal loss, $< \alpha_i >_{xy}$. If we consider a Fabry-Perot laser with the propagating mode is reflected by end mirrors, and the reflection coefficients are r_1 and r_2. respectively. In addition, the mean mirror intensity reflection coefficient, $R = r_1 r_2$.

Define the mirror lass as α_m

$$\alpha_m \equiv \frac{1}{L} \ln(\frac{1}{R}) \tag{B.7}$$

The photon decay lifetime is given by,

$$\frac{1}{\tau_p} = \frac{1}{\tau_i} + \frac{1}{\tau_m} = v_g(< \alpha_i > +\alpha_m) \tag{B.8}$$

Thus, we can also write

$$\Gamma g_{th} =< \alpha_i > +\alpha_m = \frac{1}{v_g \tau_p} \tag{B.9}$$

B.2 Threshold Current and Output Power

We construct together a below-threshold and an above-threshold characteristic to illustrate the output power versus input current for a normal diode laser. The first step is to use the below-threshold steady-state carrier rate equation,

$$\frac{\eta_i I_{th}}{qV} = (R_{sp} + R_{nr} + R_l)_{th} = \frac{N_{th}}{\tau} \tag{B.10}$$

Then, recognizing that $(R_{sp} + R_{nr} + R_l) = AN + BN^2 + CN^3$ depends monotonically on N, we observe from eq 2.34 that above threshold $(R_{sp} + R_{nr} + R_l)$ will also clamp at its threshold value, given by Eq 2.35. Thus, we can substitute Eq 2.35 into the carrier rate equation, eq 2.16 to obtain a new above threshold carrier rate equations,

$$\frac{dN}{dt} = \eta_i \frac{(I - I_{th})}{qV} - v_g g N_p, \quad (I > I_{th}) \tag{B.11}$$

We also calculate a steady-state photon density above threshold where $g = g_{th}$,

$$N_p = \frac{\eta_i (I - I_{th})}{q v_g g th V} \quad (steady\ state) \tag{B.12}$$

To obtain the power out, we first construct the stored optical energy in the cavity, E_{os}, by multiplying the photon density, N_p, by the energy per photon, hv, and the cavity volume, V_p. That is $E_{os} = N_p h v V_p$. Then, we multiply this by the erngy loss rate through the mirrors, $v_g \alpha_m = \frac{1}{\tau_m}$, to get the

optical power output from the mirrors,

$$P_0 = v_g \alpha_m N_p h v V_p \tag{B.13}$$

Substituting from , and using $\Gamma = V/V_p$,

$$P_0 = \eta_i (\frac{\alpha_m}{< \alpha_i > + \alpha_m}) \frac{hv}{q} (I - Ith), \quad (I > I_{th}) \tag{B.14}$$

For the output power below-threshold ($I < I_{th}$) can be approximated by neglecting the stimulated emission term and solving for N_p under steady-state conditions.

$$N_p = \Gamma \beta_{sp} R_{sp} \tau p \quad (I < I_{th}) \tag{B.15}$$

and

$$P_0(I < I_{th}) = \eta_r \eta_i \left(\frac{\alpha_m}{< \alpha_i > + \alpha_m} \right) \frac{hv}{q} \beta_{sp} I, \tag{B.16}$$

We can get the threshold carrier density

$$N_{th} = N_{tr} e^{g_{th}/g_0 N} = N_{tr} e^{(<\alpha_i> + \alpha_m)/\Gamma g_0 N} \tag{B.17}$$

Using the polynomial fit for the recombination rates, and recognizing that for the best laser material the recombination at threshold is dominated by spontaneous recombination, we have, $I_{th} \cong BN_{th}{}^2 qV/\eta_i$, Thus

$$I_{th} \cong \frac{qVBN_{tr}{}^2}{\eta_i} e^{(<\alpha_i> + \alpha_m)/\Gamma g_0 N} \tag{B.18}$$

where for most $III-V$ materials the bimolecular recombination coefficient, $B \sim 10^{-10} cm^3/s$.

For a multiple quantum-well (MQW) lasers, we have to multiply the single-well confinement factor, Γ_1, and volume, V_1, by the number of wells, N_w.

$$I_{thMQW} \cong \frac{qN_w V_1 B {N_{tr}}^2}{\eta_i} e^{2(<\alpha_i>+\alpha_m)/N_w \Gamma_1 g_0 N} \tag{B.19}$$

VITA

Zhihuan Wang

Place and Date of Birth: Beijing, China — 15 August 1986
Address: 3602 Hamilton St., Apt. 2, Philadelphia, PA, 19104, US
Phone: +1 (215) 2068587
email: zw78@drexel.edu

Work Experience

Present - Jun 2015
Brookhaven National Laboratory, Long Island, NY, US
Visiting Scientist
- Performed SEM/TEM imaging of as-grown and dispersed core-shell nanowires in the clean room of center for fundamental nanomaterials.
- Developed contacts of dispersed single nanowire by FIB, then characterized the device by I-V, C-V measurement and Photoluminescence spectroscopy.

Present - Mar 2012
Drexel University, Philadelphia, PA, US
Graduate Research Fellow
The focus of my research is on characterizing the extremely enhanced optical properties of core-shell nanowires and analyzing the fundamental mechanism of such significant enhancement in light absorption, emission and lasing behavior. Specifically optoelectronic characteristics and light-matter interactions of this novel nano-structure are in my interest. Meanwhile, I also participated in writing proposals for research grants from National Science Foundation, and for access permission to center for fundamental nanomaterials at Brookhaven National Lab.

Present - Mar 2012
Drexel University, Philadelphia, PA, US
Teaching Assistant
Involved dynamically in teaching responsibilities, e.g. running lectures, managing labs and carrying recitations and office hours in various courses including Electronic Devices, Analog Devices, Design for Microcontrollers, Digital Systems, Electrical Engineering Lab, Evaluation and Present Experimental Data, Linear and Dynamic Engineering System, and Statistic Analysis of Engineering System, Introduction to Physics.

Aug 2011 - Feb 2011
IM Flash Singapore LLP., Singapore
(*A Joint-Venture of Intel* and *Micron*)
Process Integration Engineer
- Written analyze report for Special Work Requests and Global Conversion to align new process recipes and tools between Singapore and US.
- Developed, maintained and improved a process module on an advance NAND Flash Memory including design rules for alternative flows.
- Optimized existing process flows and developed creative solutions to meet product requirements.
- Extracted, monitored, analyzed and reacted to inline data, param data and probe data to fix yield issues, add process margin and reduce costs.

Education

Present -	**Drexel University**, Philadelphia, PA, US
Sep 2011	Doctor of Philosophy in Electrical Engineering
	Research Field: *Solid State and Photonic Devices* — Advisor: Dr. Bahram Nabet
	Gpa: 3.93/4
Dec 2010 -	**Nanyang Technological University**, Singapore
Aug 2009	Master of Science in Electronics
	Thesis: "Numerical Characterization of Nanowire Transistors
	and Logic Gates with Parametric Variations" — Advisor: Dr. Xing Zhou
	Gpa: 4.2/5
Jun 2009 -	**Huazhong University of Science and Technology**, Wuhan, China
Sep 2005	Bachelor of Engineering in Communication Engineering
	Thesis in Chinese: "Simulation of Wireless Streaming Media Distribution
	with Performance Evaluation" — Advisor: Dr. Xu Du
	Gpa: 82/100

Awards and Certificates

2011-present	Dean's List for graduate students
	with an outstanding curriculum, Drexel University
Jan 2016	Allen Rothwarf Endowed Fellowship, Drexel University
Oct 2015	Graduate Student Domestic Travel Grant
	The Graduate College of Drexel University
Sep 2015	Finalist for Jean Bennett Memorial Student
	Travel Grant out of 200 applications, The Optical Society (OSA)
Apr 2015	Best Poster Award of Drexel IEEE Graduate Forum's
	7^{th} Annual Research Poster Symposium
Apr 2013	Best Student Poster in Physics, Drexel Research Day
Nov 2010	Best M.S. Dissertation, NTU
Aug 2009	Graduate Fellowship from Minister of Education of Singapore, NTU
May 2009	Best Engineering Undergraduate Thesis, Internet Technology
	and Engineering Research Center at HUST
Oct 2010	GRE®: 1430 (q:800;v:630) 94^{th} percentile; awa: 3.0/6.0

Publications

1. Z. Wang, B. Nabet,"Nanowire Optoelectronics" *Nanophotonics*, 4.1 (2015): -. Retrieved 17 Mar. 2016, from doi:10.1515/nanoph-2015-0025.
2. Z. Wang, B. Nabet,"Interaction of Light with Low-Dimensional Nano-cavity Structure" Submitted to Physical Review Letter, 2015.
3. Z. Wang, B. Nabet,"Light and Rate Management in Nanowires" in Frontiers in Optics 2015, OSA Technical Digest (online) (Optical Society of America, 2015), paper FW5C.6.
4. Z. Wang, M. Currie, P. Prete, N. Lovergine, B. Nabet,"Lasing from As Grown GaAs-AlGaAs Core-Shell Nanowires up to Room Temperature" in Frontiers in Optics 2015, OSA Technical Digest (online) (Optical Society of America, 2015), paper LTh2I.4.
5. Z. Wang, M. Currie, P. Prete, N. Lovergine, B. Nabet,"Room Temperature Lasing of GaAs-AlGaAs Core-Shell Nanowires Grown on Silicon Substrate" Accepted in proceeding of: 2^{nd} EOS Topical Meeting on Optics at the Nanoscale (ONS15), At Capri, Italy. Sep 17-19, 2015.
6. Z. Wang, M. Currie, P. Dianat, G. Konica, P. Prete, N. Lovergine, et al., "On Dimensional Dependence of Interaction of Light and Nano Structures," In proceeding of: Frontiers in Optics, At Orlando, FL. Oct 10-12, 2013.

7. M. Currie, Z. Wang, P. Dianat, P. Prete, I. Miccoli, N. Lovergine, et al., "Large Light Emission Enhancement in GaAs/AlGaAs CoreShell Nanowires," In proceeding of: International Conference on One-Dimensional Nanomaterials, ICON2013, At Annecy, France. Sep, 2013.
8. Zhou, X., Zhu, G. J., Srikanth, M. K., Lin, S. H., Chen, Z. H., Zhang, J. B., ... & Wang, Z. (2010). Xsim: Benchmark Tests for the Unified DG/GAA MOSFET Compact Model. Proc. Nanotech, 2, 785-788.

Poster Presentations & Panels

1. A Novel Alternative Infrastructure for Efficient High Volume Computation, Drexel IEEE Graduate Forums 7th Annual Research Poster Symposium, April, 2015.
2. Volumetric Optical Cavity Modes Allow Room Temperature GaAs/AlGaAs Core-Shell Nanowire Lasing, Drexel Research Day, April, 2014 & Nano for Business, Lehigh University, June, 2014.
3. As-grown GaAs/AlGaAs core-shell nanowire lase at room temperature, Drexel IEEE Forum, March, 2014.
4. Strong Photoluminescence Enhancement of Single GaAs/AlGaAs Core-Shell Nanowire, Drexel Research Day, April, 2013.

Languages

Chinese:	Native Proficiency
English:	Full Professional Proficiency
French:	Basic Knowledge

Research Skills

Semiconductor Fabrication and Characterization:	Photoluminescence\Electroluminescence Spectroscopy, Scanning\Atomic\Tunneling Microscopy, THz Time-Domain Spectroscopy, Electron Beam Induced Current, Low and High-Temperature Electronic Probing and e-beam Lithography
Computer:	Microsoft Excel, Word, PowerPoint, php, mySQL, html, Matlab, Meep, Python, Adobe Photoshop and Illustrator, Sketchup, Linux, ubuntu, LaTeX

Professional & Academic Membership

Starting Jun 2015	**OSA, Member**
Starting Jun 2015	**APS, Member**
Starting Aug 2013	**IEEE, Member**

Interests and Activities

Present - Aug 2015 | **Assistant Operation Officer**, Drexel IEEE Graduate (DIG)
- Served the Graduate IEEE community for contacting companies and academic professors for sponsorship and technical talks.
- Organized and served as judge for Drexel IEEE Graduate Forum's 8^{th} Annual Research Poster Symposium

Present - Aug 2015 | **First Drexel Diversity Council Advisory Board**, Student Center for Inclusion and Culture (SCIC)
- Encouraged open communication and dialogue, collaboration and promotion of inclusive programming on campus.
- Created a space where diverse student leaders collaborate and communicate with each other and the SCIC.

Technology, Open-Source, Programming
Paradoxes in Decision Making, Behavioral Finance, Stock
Basketball, Traveling, Running